

A Parallel Processing Model of the *Drosophila* Retina

Neurokernel RFC # 3 - v1.0

Aurel A. Lazar Konstantinos Psychas Nikul H. Ukani
Yiyin Zhou *

Department of Electrical Engineering
Columbia University, New York, NY 10027

August 31, 2015

Abstract

The *Drosophila* Retina has been extensively characterized in the literature in terms of structure, connectivity and function. We present here a detailed description of the algorithms required for a full-scale parallel emulation of the Retina including (i) the mapping of the visual field onto the photoreceptors, (ii) the phototransduction process, and (iii) the parallel processing of the visual field by the entire Retina. We also provide detailed algorithms, their implementation and their visual evaluation.

*Names are listed in alphabetical order.

Contents

1	Introduction	4
2	Anatomy of the <i>Drosophila</i> Retina	6
2.1	Structure of the Compound Eye	6
2.2	Structure of the Ommatidia and Photoreceptors	6
2.3	The Neural Superposition Rule	9
2.3.1	Projections of Photoreceptors into Lamina and Medulla	9
2.3.2	Neural Superposition Rule	9
3	The Visual Input to the Photoreceptors	12
3.1	The Visual Field and the Geometry of the Retina	12
3.1.1	Modeling the Geometry of the Retina	12
3.1.2	Model of the Visual Field	17
3.2	Modeling the Stimulus of a Photoreceptor as a Function of the Visual Field	18
3.3	Implementation Considerations	20
3.3.1	Hexagonal Array of Ommatidia on a Hemisphere	20
3.3.2	Generation of the Visual Stimulus	21
3.3.3	Implementation of the Computation of Photoreceptor Inputs .	23
3.4	Evaluation: Visual Acuity	23
4	I/O Characterization of Single Photoreceptors	25
4.1	The I/O Photoreceptor Model	25
4.1.1	The Photon Absorption Model	25
4.1.2	The Model of the Phototransduction Process	25
4.1.3	The Photo-Insensitive Cell Membrane Model	30
4.2	Implementation of the Photoreceptor Model	33
4.2.1	Implementation of Photo Absorption	33
4.2.2	Implementation of the Phototransduction Process	33
4.2.3	Implementation of the Photo-Insensitive Cell Membrane	35
4.2.4	Overall Implementation of the Photoreceptor Model	35
4.2.5	Complexity of the Implementation	35
4.3	I/O Evaluation of the Photoreceptor Model	36
4.3.1	Simulation Time	36
4.3.2	Transient and Steady State Responses to Constant Inputs .	36
4.3.3	Response to Natural Stimuli	36

5 The Retina as a Parallel Information Pre-Processor	38
5.1 Executing the Retina LPU in the Neurokernel	38
5.2 Distributing the Computation on Multiple GPUs	38
5.3 Visual Evaluation of the Overall Response of the Retina	40
5.3.1 Visual Characterization of the Photoreceptors	40
5.3.2 The Effect of Mean Luminance on the Retina Output	43
5.3.3 The Effect of the Speed of Motion on the Retina Output	45
6 Supplementary Videos	47
7 Acknowledgements	47
A Parameters Used in the Retina LPU Implementation	50

1 Introduction

Like other insect species, the fruit fly *Drosophila melanogaster* visually senses its environment with a pair of compound eyes. The Retina is the first layer of a compound eye that consists of $700 \sim 800$ small facets called *ommatidia*. Photoreceptors are the exclusive type of neurons hosted in the ommatidia. Therefore, the Retina is where phototransduction takes place.

The Retina can be viewed as an interface between the visual world and the visual system of the fruit fly. On the one hand, the Retina and its underlying geometry interact with the 3 dimensional visual (optical) environment. On the other hand, the Retina provides electrical signals to subsequent stages of the visual processing (the lamina and the medulla) where the retinotopy created by the structure of the compound eyes is preserved.

Each ommatidium of the *Drosophila* Retina contains 8 photoreceptors, and the total number of photoreceptors amounts to $5,400 \sim 6,400$. Although seemingly simple, each photoreceptor can perform a complex set of computations on its own [1, 2]. This suggests that the Retina is a highly parallel visual information pre-processor, partly due to the nature of the visual space, partly to provide a signal that can be processed more efficiently by subsequent processing stages.

We present in this RFC a detailed parallel processing model of the *Drosophila* Retina, including the mapping of the visual environment onto the photoreceptors as well as the phototransduction taking place inside the photoreceptors. The model is based on the structure and function of a photoreceptor that has been extensively characterized in the literature [3, 4, 1, 5]. We provide here a detailed description of the algorithms required for a full-scale parallel emulation of the Retina. This enables the study of the contribution of individual photoreceptors towards the overall spatiotemporal processing of visual scenes.

The massively parallel computational requirements of the parallel processing model mentioned above are met by the capabilities of GPU commodity hardware. The latter is the key component of the computing plane in the Neurokernel platform [6]. The simulation enables realistic inputs to be provided to models of subsequent neuropils, *e.g.*, the lamina and the medulla, thereby enabling the study of visual processing in the early vision system of the fruit fly.

This RFC is organized as follows. Retina anatomy will be discussed in Section 2. The visual input to the individual photoreceptors based on the geometry of the Retina

and visual field is modeled in Section 3. We then describe the I/O photoreceptor model in Section 4 and characterize the I/O of a single photoreceptor. Finally, in Section 5, we visually characterize the entire Retina as a parallel information pre-processor.

2 Anatomy of the *Drosophila* Retina

In this section we describe key aspects of the anatomy of the *Drosophila* Retina. The Retina is viewed here as the interface of the early visual system of the fruit fly with the external environment. The Retina model described takes into account anatomical details of the compound eye, particularly its geometric structure.

2.1 Structure of the Compound Eye

A pair of compound eyes are located, respectively, on the left and right side of the fruit fly's head. Each compound eye has a shape similar to a hemi-ellipsoid elongated along the dorsal-ventral axis. A scanning electron micrograph of the left eye is shown in Figure 1. The size of the eye is approximately $500 \mu m$ along the dorsal-ventral axis and $350 \mu m$ along the anterior-posterior axis covering a field of view of $180^\circ \times 160^\circ$ [7]. In what follows, we shall base our discussion on the left eye of the fruit fly; the structure of the right eye is mirror symmetric to that of the left eye.

The Retina of *Drosophila melanogaster* consists of $700 \sim 800$ repeated units (facets), called *ommatidia*. They are arranged precisely in a hexagonal grid (see Figure 1). Although the hemi-ellipsoid is elongated along one axis, the ommatidia array approximately spans a circular area when flattened [9]. The number of ommatidia in the central anterior-posterior row and that in the central dorsal-ventral column is about the same. The central anterior-posterior row defines the *equator* of the eye; it reveals a mirror symmetry in the configuration of photoreceptors between ommatidia above the equator and those below the equator (see also Section 2.2).

2.2 Structure of the Ommatidia and Photoreceptors

Each ommatidium in fruit fly's Retina consists of [11]

- a corneal lens and a pseudocone serving as lens elements,
- 8 photoreceptors,
- pigment cells and cone cells serving as support cells.

Each photoreceptor is divided into a photo-insensitive basal membrane and a photo-sensitive membrane [10]. A schematic drawing of a photoreceptor is illustrated in

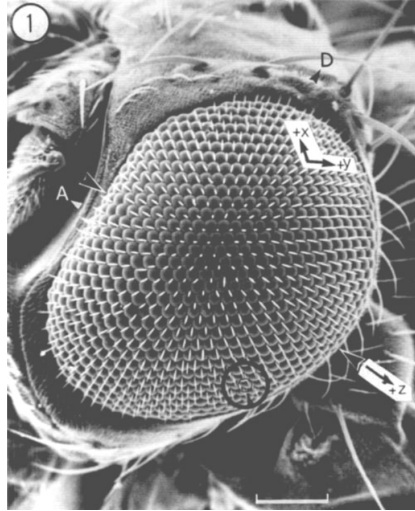


Figure 1: Scanning electron micrograph of the head of a female wild-type *Drosophila melanogaster* viewed from the left side. Magnification x145; scale bar 100 μm . Arrow A points to the anterior direction and arrow D point to the dorsal direction. (From [8], ©1991 Wiley)

Figure 2a. The photo-sensitive part is organized into tightly packed microvilli that together form a structure called *rhabdomere*. The rhabdomere is 1–2 μm in diameter and extends 100 μm along the length of the ommatidium (see also the “rhabdomere” in Figure 2b). Each rhabdomere hosts approximately 30,000 microvilli, each 1–2 μm long and 60 nm in diameter [12]. The rhabdomeres also function as waveguides such that incident light focused by the lens can pass along the length of the rhabdomeres to be absorbed by the microvilli.

In *Drosophila*, as in many other dipteran species, the 8 photoreceptors are packed into an ommatidium in a specific pattern. A schematic diagram of the structure of an ommatidium is shown in Figure 2b. First, in cross section, the rhabdomeres of all the photoreceptors (in black in Figure 2b) are located closer to the center of ommatidium while their photo-insensitive membranes occupy a larger area located peripherally. The rhabdomeres of the photoreceptors form a small hexagonal array with an asymmetric trapezoidal shape. This configuration is shown in Figure 2b for an ommatidium above the equator. On the periphery of this hexagonal array are the 6 photoreceptor cells. These photoreceptors are labeled as R1-R6, respectively. Two more rhabdomeres are stacked one on top of each other and are located in the center of the ommatidium. The photoreceptor whose rhabdomere is on the top is labeled as R7 and the other is labeled as R8. The location of rhabdomeres/photoreceptors are exactly mirror symmetric with respect to the equator.

Each rhabdomere has its own optical axis. The optical axis of a rhabdomere in an ommatidium is the extended line segment between the tip of the rhabdomere

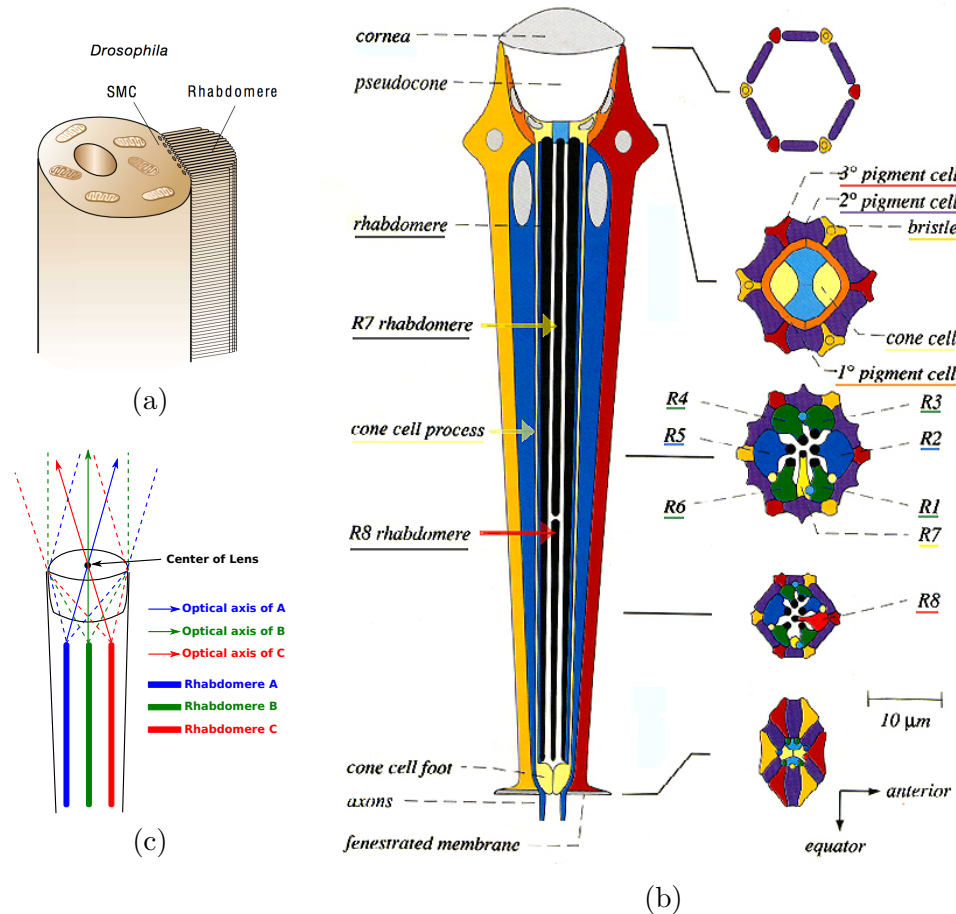


Figure 2: (a) Structure of a photoreceptor. The photosensitive rhabdomere on the right is comprised on 30,000 toothbrush bristle like microvilli. The rhabdomere is attached to a photo-insensitive membrane shown on the left. (Adapted from [10], ©2001 Nature Publishing Group)
 (b) Structure of an ommatidium. (From [11], ©1993 Cold Spring Harbor Laboratory Press)
 (c) The optical axes of different rhabdomeres in an ommatidium. Three rhabdomeres are schematically shown with thick lines in blue, green and red, respectively. Their respective optical axes are shown with arrows of the corresponding colors. The incident light parallel to the each optical axis is focused by the lens elements onto the rhabdomere.

and the center of the ommatidial lens. The corneal lens and pseudocone focus the incident light parallel to the optical axis onto the rhabdomere, as schematically shown in Figure 2c. The visual space is sampled at a resolution that is determined by the angular difference between two neighboring ommatidia also referred to as the *interommatidial angle*. The interommatidial angle $\Delta\psi$ is defined as the angular

difference between optical axes of R7/R8 in two neighboring ommatidia. In the fruit fly it is typically 5° .

2.3 The Neural Superposition Rule

2.3.1 Projections of Photoreceptors into Lamina and Medulla

Photoreceptors can be divided into two groups based on the terminal of their projections. Photoreceptors R1-R6 form the first group projecting directly to the first visual neuropil, the Lamina, while R7 and R8 form the second group that bypasses (and has no synaptic interaction in) the Lamina and projects directly to the Medulla, the second visual neuropil [8]. The two groups are also functionally distinct as R1-R6 are mainly used for “black-and-white” vision, while R7 and R8 are responsible for color.

In the Lamina and the Medulla, repeating structures similar to the ommatidia preserve the hexagonal arrangement and retinotopy from the Retina. The repeating elements are respectively called cartridges and columns in the Lamina and the Medulla. There is always a cartridge and a column for each ommatidium sharing the same relative position in the hexagonal grid. We refer to them as the corresponding cartridge and the corresponding column, respectively, of the ommatidium.

R7 and R8 in an ommatidium project their axons to the corresponding column in the Medulla. This is not the case, however, for R1-R6. The projection of R1-R6 to the Lamina follows the neural superposition rule [3], which we will briefly describe next.

2.3.2 Neural Superposition Rule

Each of the photoreceptors R1-R6 in an ommatidium projects to a different cartridge in the Lamina. In turn, each cartridge is innervated by axon terminals of 6 photoreceptors, that each belong to a different ommatidium. The rule of this projection pattern is governed by the optical axes of the rhabdomeres of the photoreceptors.

R1-R6 and R7/R8 in the same ommatidium have different optical axes. The optical axes of the R7/R8 photoreceptors of three neighboring ommatidia are shown on top-right in Figure 3a in gray dashed lines. The rhabdomeres of R7/R8 in an ommatidium

share their optical axis with that of R1-R6, each located in a different neighboring ommatidia. Those photoreceptors sharing the same optical axis are highlighted in red in Figure 3b. This pattern resembles the trapezoidal arrangement of the individual photoreceptors in a single ommatidium. This occurs in a repetitive pattern, and it is easy to see that this pattern tiles the entire ommatidia array. The optical axes of three photoreceptors with a common direction located in adjacent ommatidia are shown with the directed red lines in Figure 3a.

The neural superposition rule can then be simply described as the following: photoreceptors R1-R6 that share the same optical axis project to one cartridge in the Lamina, and the target cartridge is the corresponding cartridge of the ommatidium where R7/R8 with the same optical axis reside. Moreover, the R7/R8 project to the corresponding column in the Medulla. Therefore, the neural superposition rule guarantees the tiling of the ommatidia array by the corresponding cartridges and columns array. See also Figure 3c.

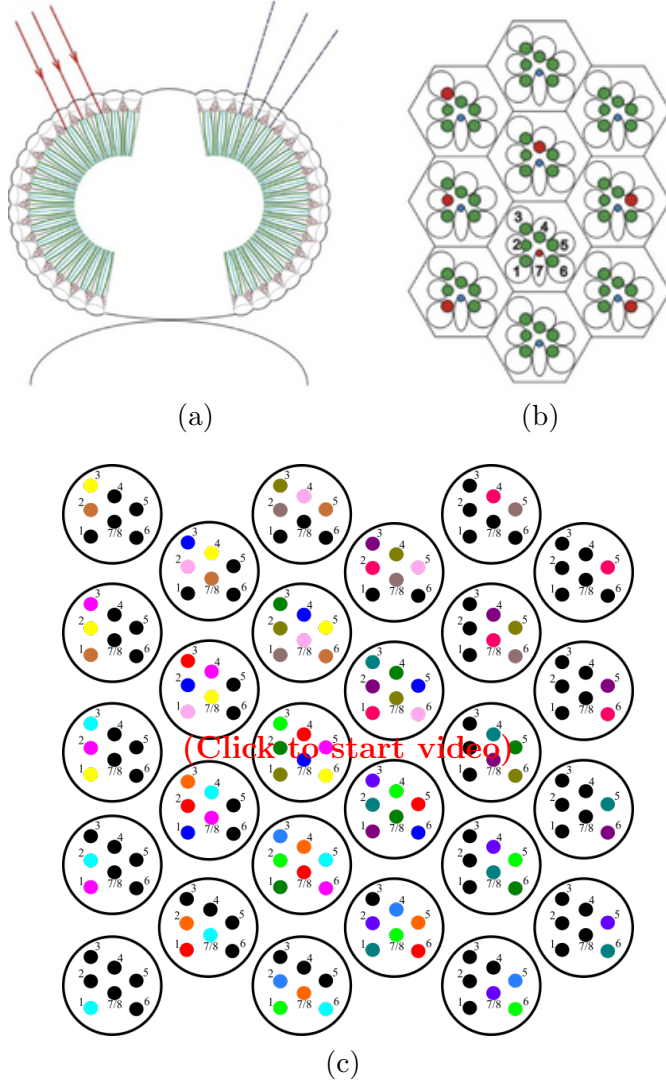


Figure 3: (a) The interommatidial angle difference between optical axes (the angle between gray dashed lines) is about 5° in the fruit fly. (b) Red cells have optical axes with a common direction, as shown with the directed red lines in (a). ((a) and (b) are modified from [13], ©2008 Stavenga and Arikawa) (c) A video showing the tiling of the neural superposition pattern. Photoreceptors (represented by dots) of the same color (except for black) have parallel optical axes. Note that the 5 ommatidia that tile the center of the figure/video each have all photoreceptors filled with color. The unfilled dots (black) remaining in the other ommatidia are on the boundary. As the latter grows, so does the tiled center. (To enable the video, see Supplementary Videos in Section 6.)

3 The Visual Input to the Photoreceptors

In this section, we describe the visual input to single photoreceptors.

3.1 The Visual Field and the Geometry of the Retina

3.1.1 Modeling the Geometry of the Retina

In section 2.1 we mentioned that the fly eye has an ellipsoidal shape and a field of view that is 180° in almost all directions. To simplify the analysis below, we model the surface of the Retina as a hemisphere; w.l.o.g., the hemisphere has unit radius. Ommatidia are positioned on the hemisphere in such a way that they cover the entire field of view and, ideally, they form a hexagonal array.

It is, however, not possible to construct an exact hexagonal array on a hemisphere. We obtain a good approximation by first constructing an exact hexagonal array on a 2-dimensional plane and then by projecting the latter array onto the hemisphere by using the Albers equal-area conic projection [14].

Indexing the Ommatidia Array

We consider an array of ommatidia on a 2D plane. For simplicity, each hexagon (ommatidium) is represented by a circle (see Figure 4). The indexing or numbering scheme of the ommatidia array is provided by an index (r, s, l) , where r is the layer index, s is the section index and l is the local index.

First, we note that the ommatidia array in Figure 4 can be seen as a set of concentric hexagons, called layers. Each of these layers is assigned a different color in the same figure. The indexing of the ommatidia starts with the labeling of the layers. Layer 0 consists of a single ommatidium that is located at the center of the plane (see also Figure 4a). Layer 1 consists of the 6 ommatidia that wrap layer 0, layer 2 consists of the 12 ommatidia that wrap layer 1, and so on. Second, all the ommatidia that belong to similarly oriented edges of the concentric hexagons (layers) are assigned the same section index (see Figure 4b). Finally, we assign a local index to each ommatidium with the same layer and section index. The local index l takes values from 0 to $r - 1$, where r is the layer index. $l = 0$ is assigned to the ommatidium located at the vertex of a layer and increases clockwise (see also Figure 4c).

The reason for choosing this indexing scheme is two-fold. First, by using concentric

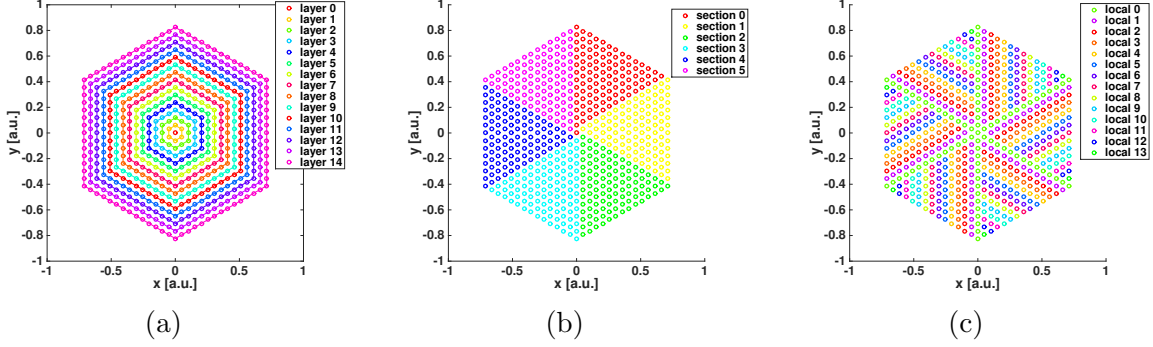


Figure 4: Construction of the ommatidia array on a 2D plane and the numbering scheme. (a) Layers 0 to 14, that form concentric hexagons around the origin, are first placed onto the 2D plane. (b) Section index for ommatidia in the hexagonal array (c) Local index for ommatidia.

hexagonal layers, the indexing scheme naturally fits into a circular area. Second, when using a single number to index the ommatidia, the index is consistent regardless of how many layers are used (see also (10)).

We denote the distance between the center points of two neighboring ommatidia as d . Then, the position of each center point on the 2D plane can be expressed as

$$(x, y) = \begin{cases} \left(\frac{\sqrt{3}}{2}d \cdot l, d \cdot \left(r - \frac{1}{2}l\right) \right), & \text{if } s = 0, \\ \left(\frac{\sqrt{3}}{2}d \cdot r, d \cdot \left(\frac{1}{2}r - l\right) \right), & \text{if } s = 1, \\ \left(\frac{\sqrt{3}}{2}d \cdot \left(r - l\right), -\frac{1}{2}d \cdot \left(r + l\right) \right), & \text{if } s = 2, \\ \left(\frac{-\sqrt{3}}{2}d \cdot l, d \cdot \left(\frac{1}{2}l - r\right) \right), & \text{if } s = 3, \\ \left(\frac{-\sqrt{3}}{2}d \cdot r, d \cdot \left(l - \frac{1}{2}r\right) \right), & \text{if } s = 4, \\ \left(\frac{\sqrt{3}}{2}d \cdot \left(l - r\right), \frac{1}{2}d \cdot \left(r + l\right) \right), & \text{if } s = 5. \end{cases} \quad (1)$$

The choice of d and the resulting total number of layers must be such that all the ommatidia are placed within a unit circle. Then, by using the projection scheme described next, the ommatidia array in the unit circle can be properly projected onto the unit hemisphere.

Projection onto Hemisphere

Using the inverse Albers projection, we map the ommatidia array defined above onto the surface of the hemisphere. For the hemisphere, we use the spherical coordinate system with coordinates $(\rho', \theta', \varphi')$, where ρ' is the distance from the origin, θ' is the

azimuth angle, and φ' is the zenith angle. Assuming $\rho' = 1$, the hemisphere surface is $\theta' \in [0, 2\pi]$, $\varphi' \in [0, \pi/2]$ (see also Figure 5(a)).

The inverse Albers projection maps an arbitrary point (x, y) inside a unit circle on the 2D plane to a point (θ', φ') on the surface of the hemisphere by

$$\begin{aligned}\theta' &= \arctan2(y, x), \\ \varphi' &= \arccos(1 - x^2 - y^2).\end{aligned}\tag{2}$$

Note that any point outside the unit circle will either be projected to the lower hemisphere surface with $\varphi' > \pi/2$, or be outside the domain of \arccos . The equation (2) above maps/projects the origin of the 2D plane to the north pole of the hemisphere. The map is an equal area map projection from the unit circle to the hemisphere surface.

Horizontal Coordinate System

The hemisphere we introduced above faces upwards. The hemisphere corresponding to the left eye is obtained by its rotation around the x-axis by 90 degrees. Note that the right eye is mirror symmetric to the left eye in terms of the neural superposition rule. In addition, we use the horizontal coordinate system in representing the surface of the rotated hemisphere, where $\theta \in [0, \pi]$ is the azimuth (one eye only sees 180° from front to back), and $\varphi \in [-\frac{\pi}{2}, \frac{\pi}{2}]$ is the elevation. The horizontal coordinate system is illustrated in Figure 5b.

We first performed a change of coordinate for the upward-facing hemisphere surface from the spherical coordinate system to the Cartesian coordinate system, and then rotated it by 90°. An arbitrary point (θ', φ') on the upward-facing hemisphere surface is mapped to (x', y', z') on the rotated hemisphere surface by

$$\begin{bmatrix} x' \\ y' \\ z' \end{bmatrix} = \begin{bmatrix} 1 & 0 & 0 \\ 0 & 0 & -1 \\ 0 & 1 & 0 \end{bmatrix} \begin{bmatrix} \sin \varphi' \cos \theta' \\ \sin \varphi' \sin \theta' \\ \cos \varphi' \end{bmatrix},\tag{3}$$

and therefore, we have

$$\begin{aligned}x' &= \sin \varphi' \cos \theta' \\ y' &= -\cos \varphi' \\ z' &= \sin \varphi' \sin \theta'.\end{aligned}\tag{4}$$

Finally, a change of coordinate from (x', y', z') in the Cartesian coordinate system to

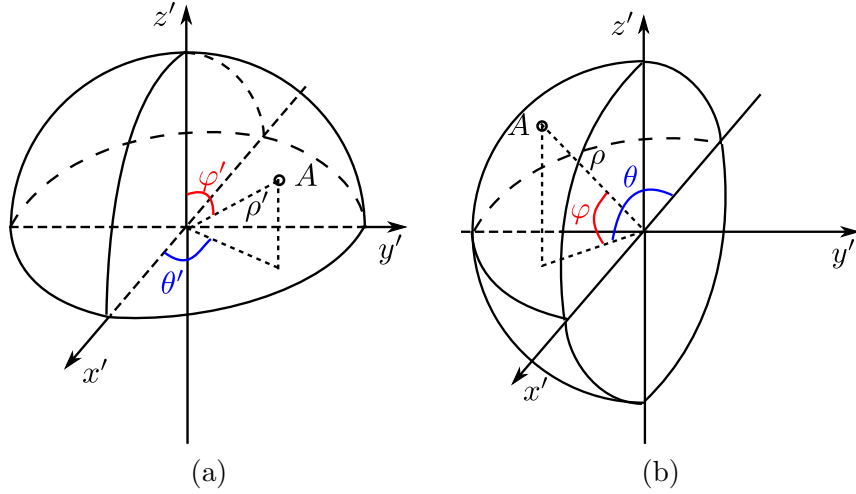


Figure 5: (a) The spherical coordinate system. A point A on the surface of a upward-facing hemisphere ($\rho' = 1$) is represented by the azimuth θ' and the zenith angle φ' . (b) The horizontal coordinate system. A point A on the surface of a unit hemisphere ($\rho = 1$) is represented by the azimuth θ and the elevation φ . Note that by choice, $\theta = 0$ starts from the negative x' -axis, and the left eye covers $\theta \in [0, \pi]$.

(θ, φ) in the horizontal coordinate system is given by

$$\begin{aligned}\theta &= \arctan2(-y', -x') \\ \varphi &= \arcsin\left(\frac{z'}{\sqrt{x'^2 + y'^2 + z'^2}}\right),\end{aligned}\quad (5)$$

An arbitrary point on the surface of the rotated hemisphere in the horizontal coordinate system can be directly related to a point on a unit circle on the original 2D plane by combining (2), (4) and (5), and can be expressed as

$$\begin{aligned}\theta &= \arctan2\left((1 - x^2 - y^2), -\sqrt{1 - (1 - x^2 - y^2)^2} \cos(\arctan2(y, x))\right) \\ \varphi &= \arcsin\left(\sqrt{1 - (1 - x^2 - y^2)^2} \sin(\arctan2(y, x))\right).\end{aligned}\quad (6)$$

The resulting ommatidia array with 721 ommatidia is shown in the video in Figure 6 (see also Section 3.3.1 for details of the generation of the ommatidia array).

Ideally, the photoreceptors in an ommatidium are physically located in different positions (see Figure 3b). For simplicity, on the hemisphere surface, however, they are all assumed to be positioned at the center of the ommatidium.

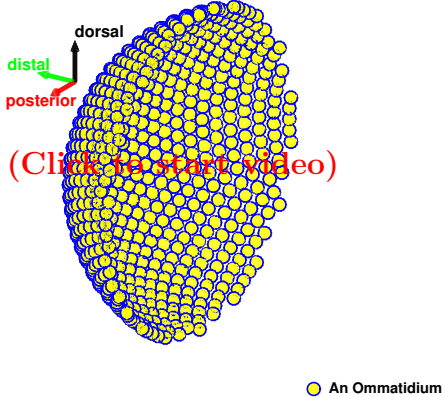


Figure 6: An array of 721 ommatidia positioned on the retina of the right eye modeled as a hemisphere. Dorsal, distal and posterior directions are indicated by the coordinate system on the top right. Each yellow circle represents the position of an ommatidium. (To enable the video, see Supplementary Videos in Section 6.)

Optical Axes

The neural superposition rule described in section 2.3.2 determines a set of photoreceptors that have optical axes parallel to each other. Here, we establish the optical axis of each single photoreceptor in the Retina model.

We first define the optical axis of R7 in an ommatidium as the normal vector at the center of the ommatidium on the hemisphere. Given the coordinate of the ommatidium (θ, φ) in the horizontal coordinate system, the normal of the ommatidium on the hemisphere surface can be expressed as the Cartesian vector

$$\mathbf{n} = [-\cos \varphi \cos \theta, -\cos \varphi \sin \theta, \sin \varphi]^T, \quad (7)$$

where $[\cdot]^T$ denotes the transpose.

Optical axes parallel to that of the R7 photoreceptor are assigned to R1-R6 in 6 different ommatidia so that the superposition rule is satisfied. For example, Figure 7a shows the parallel optical axes of the 6 photoreceptors. The resulting optical axes of photoreceptors in the same ommatidium is shown in Figure 7b.

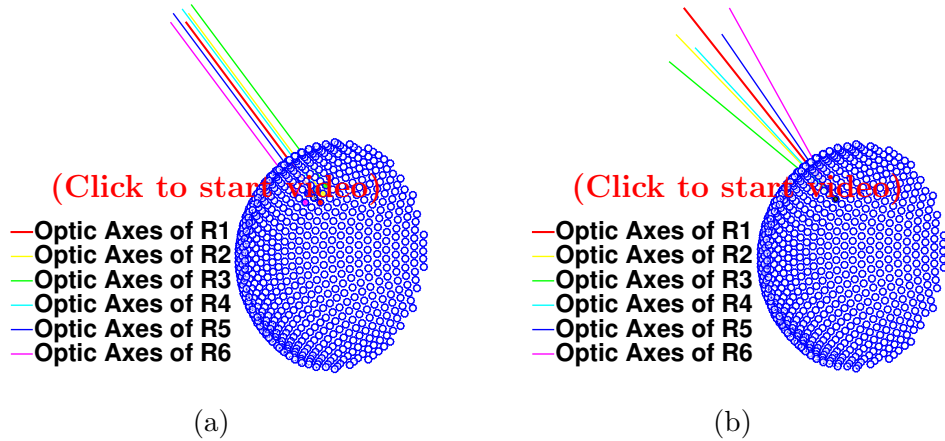


Figure 7: Optical axes of photoreceptors under the neural superposition rule. (a) Optical axes of 6 photoreceptors from 6 different ommatidia that have parallel optical axes. Red dot on the ommatidia array shows the ommatidium where R1 is positioned. Ommatidia in other colors (in legend) contribute R2, R3, R4, R5 and R6, respectively, to the set of photoreceptors having the same optical axes. (b) Optical axes of photoreceptors from the same ommatidium. (To enable the video, see Supplementary Videos in Section 6.)

3.1.2 Model of the Visual Field

Visual stimuli presented to the eyes in a natural environment arise from the reflection, refraction and diffraction of light from light sources by the objects in the environment. The most realistic simulation of visual stimuli typically requires creating a virtual 3D environment and performing ray tracing to calculate the path of light waves to the eye. This technique, while desirable, is computationally very demanding.

In this RFC, we take a simpler approach to ray tracing that is computationally less intensive. The visual field is modeled as a screen surrounding the eye in the 3D space. The screen is viewed as a light source that can have either a hemi-spherical (see Figure 8a) or cylindrical (see Figure 8b) shape. These setups, particularly the one offered by the cylindrical screen, are akin to those used in experiments [15]. At the same time, the geometrical relationship between the light sources and the eye is largely kept the same.

We first describe the visual field defined on a hemisphere. The coordinate system is chosen to be the horizontal coordinate system shown in Figure 8a. For a fixed

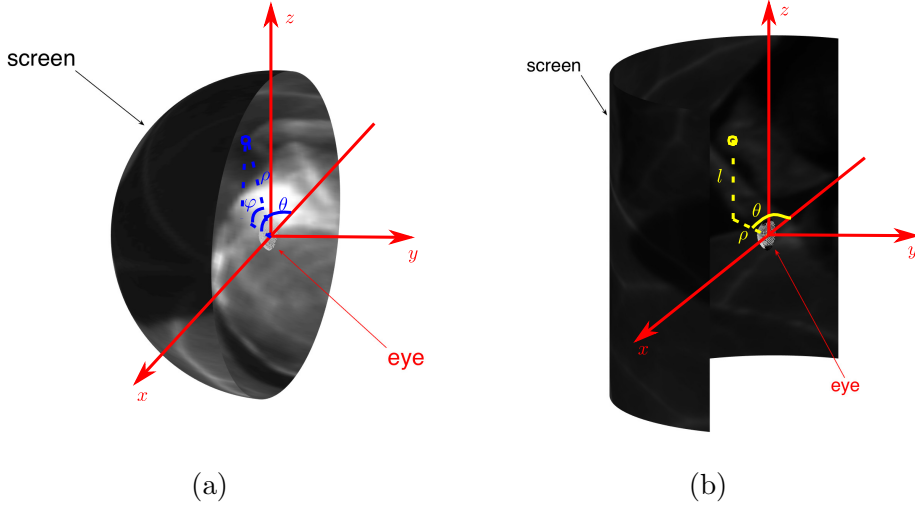


Figure 8: Relative position between the screen and the eye. (a) Hemi-spherical screen and the associated horizontal coordinate system. (b) Cylindrical screen and the associated cylindrical coordinate system.

radius ρ , stimuli defined on the hemispherical screen are denoted by $u(\theta, \varphi, t)$, where $\theta \in [0, \pi]$ is the azimuth, and $\varphi \in [-\frac{\pi}{2}, \frac{\pi}{2}]$ is the elevation (see also Figure 8a).

The cylindrical screen is defined under a cylindrical coordinate system as shown in Figure 8b. With a fixed radius ρ , stimuli are denoted, by abuse of notation, as $u(\theta, l, t)$, where $\theta \in [0, \pi]$ is the azimuth and $l \in [-L, L]$ is the height of the cylinder. Elevation φ can then be defined as $\varphi = \arctan(l/\rho)$. Note, however, that here the elevation is not defined on the surface of a hemisphere.

In the rest of this RFC, we will focus on a visual field defined on the hemispherical screen. Visual fields on the cylindrical screen can be similarly obtained.

3.2 Modeling the Stimulus of a Photoreceptor as a Function of the Visual Field

A photoreceptor is not only sensitive to a point source located on the path of its optical axis, but also to the visual space surrounding the optical axis up to a certain angle. This is mainly due to the combined effect of the diffraction of the lens and the width of its rhabdomere.

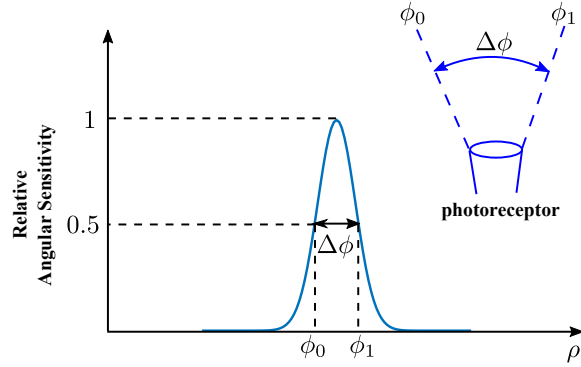


Figure 9: Graphical representation of the acceptance angle $\Delta\phi$ in one dimension.

The angular sensitivity can be well approximated by a Gaussian function whose half-width is called the *acceptance angle* $\Delta\phi$ [16], as depicted in Figure 9. For Drosophila, this value is about 8.2° [17]. We use a linear filter to account for the effect of angular sensitivity on the visual field at the input to a photoreceptor. Given that the visual field is defined on a hemisphere, the linear filter is modeled as a Von Mises-Fisher distribution, the sphere analogue of the normal distribution. For the i th photoreceptor whose optical axis intersects with the spherical screen at (θ^i, φ^i) , its filter is of the form

$$h^i(\theta, \varphi) = \frac{\kappa}{2\pi(e^\kappa - e^{-\kappa})} e^{\kappa \cos \phi}, \quad (8)$$

where $\kappa = \frac{\log 2}{1-\cos(\Delta\phi/2)}$, and ϕ is the angle between the vectors $(\rho, \theta^i, \varphi^i)$ and (ρ, θ, φ) , and

$$\cos \phi = \cos \varphi \cos \varphi^i \cos(\theta - \theta^i) + \sin \varphi \sin \varphi^i.$$

To see the above, transform unit vectors $(1, \theta^i, \varphi^i)$ and $(1, \theta, \varphi)$ to Cartesian coordinates and take the inner product between the two:

$$\begin{aligned} \cos \phi &= \langle (-\cos \varphi \cos \theta, -\cos \varphi \sin \theta, \sin \varphi), (-\cos \varphi^i \cos \theta^i, -\cos \varphi^i \sin \theta^i, \sin \varphi^i) \rangle \\ &= \cos \varphi \cos \varphi^i (\cos \theta \cos \theta^i + \sin \theta \sin \theta^i) + \sin \varphi \sin \varphi^i \\ &= \cos \varphi \cos \varphi^i \cos(\theta - \theta^i) + \sin \varphi \sin \varphi^i. \end{aligned}$$

An example filter of a photoreceptor is shown in Figure 10.

Therefore, for a visual field $u(\theta, \varphi, t)$, the Poisson rate of photons at the input to the i th photoreceptor can be expressed as

$$\lambda^i(t) = \int_{-\frac{\pi}{2}}^{\frac{\pi}{2}} \int_0^\pi h^i(\theta, \varphi) u(\theta, \varphi, t) \cos \varphi d\theta d\varphi. \quad (9)$$

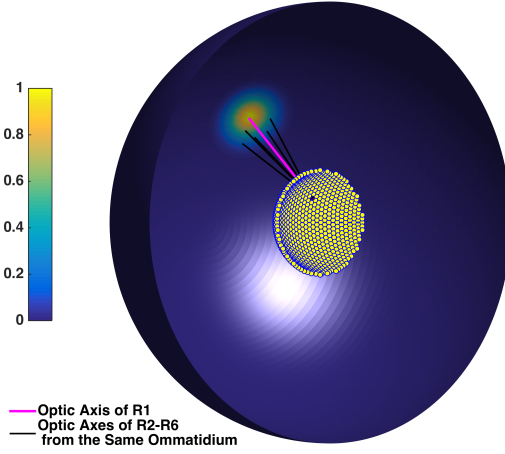


Figure 10: Receptive field of a photoreceptor. The ommatidia array is shown by yellow dots. The outer hemisphere shows, on the visual field, the filter of the R1 photoreceptor of the ommatidium shown in black. The strength of the filter is color coded using the colorbar on the left. The optical axis of the R1 neuron is shown in magenta, while optical axes of the rest of photoreceptors in the same ommatidium are shown in black. Note that the filter for R1 is centered at the intersection of its optical axis (magenta line) and the screen.

Note that the surface element on a sphere is $\rho^2 \cos \varphi d\theta d\varphi$. The ρ^2 term is safely ignored.

3.3 Implementation Considerations

3.3.1 Hexagonal Array of Ommatidia on a Hemisphere

In section 3.1.1, we defined the indexing of ommatidia in the hexagonal array by a ring index, section index and local index. Here, to facilitate the indexing in implementation, we employ an ommatidium index i that uniquely identifies each ommatidium. The index i is related to layer, section and local index (r, s, l) by

$$i = 3r(r + 1) + rs + l. \quad (10)$$

This index will be used to specify a port name for each photoreceptor in Section 5.1. Assuming that a total of N layers are used to construct the ommatidia array on the 2D plane, additional ommatidia that belong to layer r , $r > N$ are padded to fill a circular area (see black circles in Figure 11). The distance to the origin of the padded

ommatidia is less than the maximum distance to the origin of ommatidia in layer N .

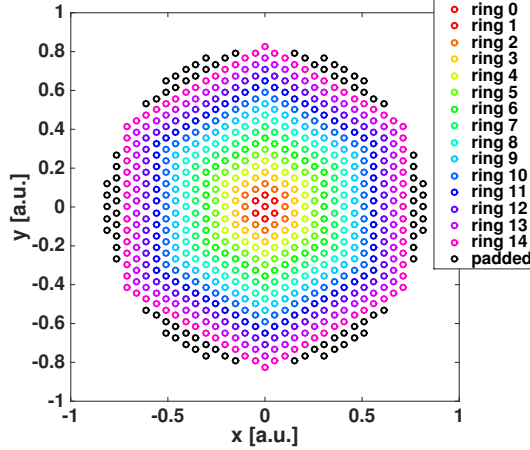


Figure 11: Construction of an ommatidia array on a 2D plane. Layers 0 to 14, that form concentric hexagons around the origin with increasing distance, are first placed onto the 2D plane. Additional ommatidia (black) are padded outside layer 14 in order to fill a circular area.

The creation of the ommatidia array is described in Algorithm 1.

3.3.2 Generation of the Visual Stimulus

In order to generate stimuli on a hemisphere screen, videos are first created in the (x, y) domain and then mapped onto the hemisphere screen by (6). Stimuli are generated in this way since most natural videos taken by a camera are in Cartesian coordinates. A more desirable way to create videos is to use a fisheye lens when taking videos.

The procedure for generating stimuli on a hemispherical screen is described in Algorithm 2. The stimulus is generated on a discrete grid on the hemisphere, *i.e.*, $\theta \in [0, \pi]$ is uniformly discretized into N_θ points with $\theta_m = m\frac{\pi}{N_\theta}$, $m = 0, 1, 2, \dots, N_\theta - 1$, and $\varphi \in [-\frac{\pi}{2}, \frac{\pi}{2}]$ is uniformly discretized into N_φ points with $\varphi_n = n\frac{\pi}{N_\varphi} - \frac{\pi}{2}$, $n = 0, 1, 2, \dots, N_\varphi - 1$. We denote the i th frame of the stimulus on the discrete hemisphere surface as $u_i[m, n] = u(\theta_m, \varphi_n, i\Delta t)$, where Δt is the time between two consecutive frames.

Algorithm 1 Creation of Hexagonal Array of Ommatidia

```

procedure HEXAGONAL_ARRAY( $\#layers$ )
     $\#padded.layers \leftarrow \#layers + 3$ ,
     $d \leftarrow \frac{1}{\#padded.layers}$ ,
    create layer 0 at the origin,
    for  $i \leftarrow 1, \#padded.layers$  do
        add layer  $i$  with distance  $d \cdot i$ , a total of  $6i$  points added.
    end for
    Extract all points whose distance to origin is smaller than  $\#layers \cdot d$ ,
    Map points on 2D plane to hemisphere of radius 1 using (6).
    Compute the normal of each ommatidia position by (7).
    Assign the normal to optical axes to R1-R6 according to neural superposition
    rule.
end procedure

```

Algorithm 2 Generate stimuli on hemisphere screen from 2D videos

```

procedure STIMULI
    for  $i \leftarrow 1, \#frames$  do
        Generate  $i$ th frame  $\hat{u}_i(x, y)$ ,
        Using the inverse of (6), map the points  $(\theta_m, \varphi_n), m = 1, \dots, N_\theta, n =$ 
         $1, \dots, N_\varphi$  of the screen grid to the image coordinates  $(x_m, y_n)$ ,
         $\hat{u}_i(x_m, y_n) \leftarrow \text{Interpolate}(\hat{u}_i(x, y), x_m, y_n)$ 
         $u_i[m, n] \leftarrow \hat{u}_i(x_m, y_n)$ .
    end for
end procedure

```

3.3.3 Implementation of the Computation of Photoreceptor Inputs

The filter of each photoreceptor is computed on the same discrete grid as the generated stimulus. We denote the filter of i th photoreceptor as $h^j[m, n] = h^j(\theta_m, \varphi_n)$, $m = 1, 2, \dots, N_\theta$, $n = 1, 2, \dots, N_\varphi$. The inputs $\lambda_i^j = \lambda^j(i\Delta t)$ to photoreceptor j at i th frame is then computed using Algorithm 3.

Algorithm 3 Compute inputs to photoreceptors

```

procedure FILTERING( $u_i$ )
  for  $j \leftarrow 1, \#photoreceptors$  do
     $h^j[m, n] \leftarrow h^j(\theta_m, \varphi_n)$ ,  $m = 1, 2, \dots, N_\theta$ ,  $n = 1, 2, \dots, N_\varphi$ ,
     $\lambda_i^j \leftarrow \sum_{m,n} u_i[m, n] h^j[m, n] \cos(\varphi_n) \frac{\pi}{N_\theta} \frac{\pi}{N_\varphi}$ .
  end for
end procedure

```

3.4 Evaluation: Visual Acuity

To evaluate the visual inputs to the photoreceptors, we used natural images from the van Hateren dataset [18]. The images in the dataset are raw images whose values are proportional to the luminance (number of photons).

We created a circular window (in red) on the 2D image and moved it to simulate the movement of the fly. The image within the circular window was projected onto the hemispherical screen by Algorithm 2. The top-down view of the screen is shown in the second row of Figure 12 on the left.

To study the effect of the acceptance angle $\Delta\rho$, we used 3 different values, $\Delta\rho = 5^\circ$, $\Delta\rho = 8^\circ$ and $\Delta\rho = 11^\circ$. The resulting visual inputs to the photoreceptors are shown in Figure 12. A wider angular sensitivity results in a more blurry input to the photoreceptors, limiting the visual acuity of the eyes.

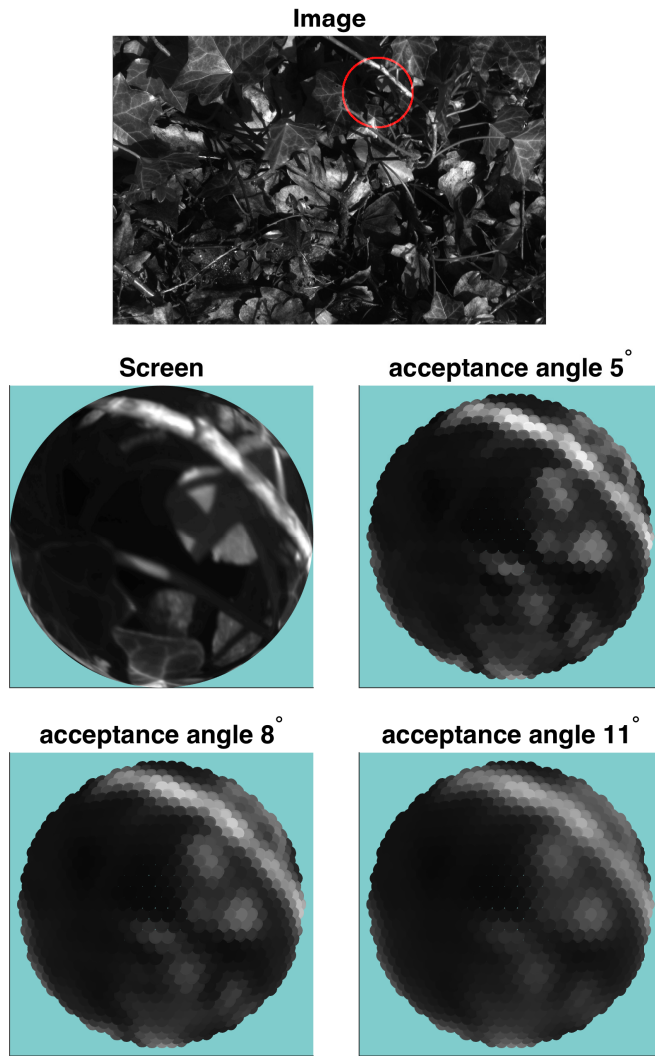


Figure 12: Visual input to the photoreceptors. A visual scene is generated based on a 2D image (Image). A circular window (red) moving across the image depicts/corresponds to the movement of the fly. The image within the circular window is projected on to the visual screen of the Retina model (Screen). After filtering the stimulus with the filter of the photoreceptors, the input to the R1 photoreceptors is shown in their respective ommatidia (acceptance angle 8°). Two different acceptance angles are also used for comparison (acceptance angle 5° and acceptance angle 11°).

4 I/O Characterization of Single Photoreceptors

4.1 The I/O Photoreceptor Model

Here, we describe an I/O photoreceptor model that closely follows [1, 19]. The photoreceptor model consists of 3 parts, namely, a photon absorption model, a photo-transduction process model and finally a photo-insensitive cell membrane model.

4.1.1 The Photon Absorption Model

The number of photons absorbed by the j th photoreceptor, $j = 1, 2, \dots, N$, is a Poisson process with rate $\lambda^j(t)$, where $\lambda^j(t)$ is the input to photoreceptor j in (9). Assuming that each microvillus has an equal probability of absorbing a photon arriving at the photoreceptor, the number of photons absorbed by each microvillus is a Poisson process with rate $\lambda_m^j(t) = \frac{\lambda^j(t)}{M}$, $m = 1, 2, \dots, M$, $j = 1, 2, \dots, N$. Here M is the number of microvilli in the photoreceptor's rhabdomere.

4.1.2 The Model of the Phototransduction Process

The process of phototransduction converts light into electrical signals, as mentioned earlier. The details of this process can be found in [19] and are visually presented in Figure 13.

First, photons are absorbed by the microvilli of the photoreceptors. This initiates a reaction cascade that starts with the activation of rhodopsin and ultimately leads to an ion exchange across the membrane that results in a current flow. Each microvillus generates small current bumps in response to the absorption of photons. The aggregation of the outputs of all microvilli produces a macroscopic current.

Each of the microvilli has about $\sim 1,000$ rhodopsin molecules [21, 22]. That means that at any given time a microvillus cannot absorb more photons than the number of non excited rhodopsin molecules contained in it.

Next we will give a brief description of the equations that model the phototransduction process. For detailed description of constants and variables used, the reader should kindly refer to section A of the Appendix.

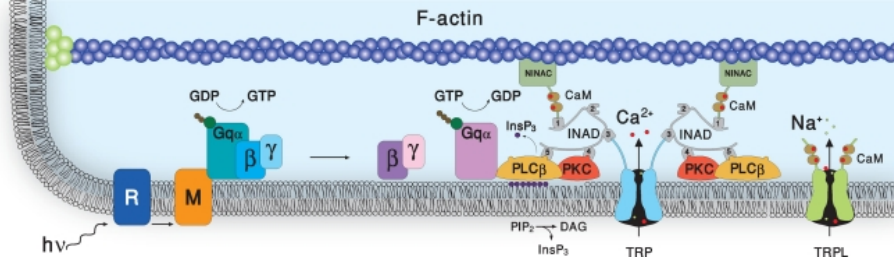


Figure 13: Phototransduction cascade. A photon ($h\nu$) activates a rhodopsin (R) that turns into metarhodopsin (M). The metarhodopsin then activates a second messenger, G-protein ($G_{q\alpha}$), by promoting the GDP to GTP exchange. GTP then catalyzes the phospholipase $C\beta$ ($PLC\beta$). G-protein coupled PLC cleaves phosphatidyl 4,5-bisphosphate (PIP_2) into two intracellular messengers: inositol trisphosphate ($InsP_3$) and diacylglycerol (DAG). Subsequently, TRP and $TRPL$, two light-sensitive channels, open. The opening of these transduction-channels fluxes in permeable ions, Na^+ , Ca^{2+} , Mg^{2+} , generating current inside a single microvillus [20, 19] (From [20], ©2009 Katz and Minke).

We denote the molecules and ions involved in the phototransduction process with the variable names listed below. A variable without square brackets denotes the number of molecules/ions, one with square brackets, *e.g.*, $[Ca^{2+}]_i$, denotes the intracellular concentration of the molecule/ion, whereas $[Ca^{2+}]_o$ denotes the extracellular concentration of Calcium.

- x_1 : M^* , metarhodopsin (to be distinguished from M , the number of microvilli in each photoreceptor)
- x_2 : G , G-protein state $G_\alpha G_\beta G_\gamma GDP$
- x_3 : G^* , G-protein state GTP
- x_4 : PLC^* , $G_\alpha GTP-PLC$
- $T_3 - x_4$: PLC , phospholipase C
- $T_4 - x_2 - x_3 - x_4$: $G_\alpha GDP$, guanosine diphosphate
- x_5 : D^* , diacylglycerol
- x_6 : TRP^* , number of opened $TRP/TRPL$ channels
- $T_1 - x_6$: TRP , number of closed $TRP/TRPL$ channels
- x_7 : CaM^* , Calcium bound Calmodulin
- $T_2 - x_7$: CaM , Calmodulin

- x_8 : $[Ca^{2+}]_i$, Calcium ion concentration.

where $T_1 = TRP_{total}$, $T_2 = CaM_{total}$, $T_3 = PLC_{total}$ and $T_4 = G_{total}$ are the total number of respective channels/molecules available in a microvillus. See also, Table 2, Appendix A.

For microvilli $m, m = 1, 2, \dots, M$, where M is the total number of microvilli (to be distinguished from M^* , the metarhodopsin), we define the vector stochastic process

$$\mathbf{X}^m = [X_1^m, X_2^m, X_3^m, X_4^m, X_5^m, X_6^m, X_7^m]^\top.$$

In addition, we define the scalar random process X_8^m for $[Ca^{2+}]_i$. As we will show in (15), the dynamics of $[Ca^{2+}]_i$ is fast enough such that X_8^m can be determined from \mathbf{X}^m and the membrane voltage of the photoreceptor.

We denote the probability that $\mathbf{X}^m = \mathbf{x}$, given that $\mathbf{X}_0^m = \mathbf{x}_0$ as $\mathbb{P}(\mathbf{X}^m = \mathbf{x} | \mathbf{X}_0^m = \mathbf{x}_0)$. The phototransduction process can be expressed by the following chemical master equation [23]

$$\begin{aligned} & \frac{d}{dt} \mathbb{P}(\mathbf{X}^m = \mathbf{x} | \mathbf{X}_0^m = \mathbf{x}_0) \\ &= \sum_{j=1}^{13} [S_j(\mathbf{x} - \mathbf{b}_j, V, W) \mathbb{P}(\mathbf{X} = \mathbf{x} - \mathbf{b}_j | \mathbf{X}_0^m = \mathbf{x}_0) - S_j(\mathbf{x}, V, W) \mathbb{P}(\mathbf{X}^m = \mathbf{x} | \mathbf{X}_0^m = \mathbf{x}_0)], \end{aligned} \quad (11)$$

where $\mathbf{B} = [\mathbf{b}_1, \mathbf{b}_2, \dots, \mathbf{b}_{13}]$ is the jump matrix with

$$\mathbf{B} = \begin{bmatrix} 1 & -1 & 0 & 0 & 0 & 0 & 0 & 0 & 0 & 0 & 0 & 0 & 0 \\ 0 & 0 & -1 & 0 & 0 & 1 & 0 & 0 & 0 & 0 & 0 & 0 & 0 \\ 0 & 0 & 1 & -1 & -1 & 0 & 0 & 0 & 0 & 0 & 0 & 0 & 0 \\ 0 & 0 & 0 & 1 & 0 & 0 & 0 & -1 & 0 & 0 & 0 & 0 & 0 \\ 0 & 0 & 0 & 0 & 0 & 1 & 0 & -1 & -2 & 0 & 0 & 0 & 0 \\ 0 & 0 & 0 & 0 & 0 & 0 & 0 & 0 & 1 & -1 & 0 & 0 & 0 \\ 0 & 0 & 0 & 0 & 0 & 0 & 0 & 0 & 0 & 0 & 1 & -1 & 0 \end{bmatrix},$$

and $S_j, j = 1, 2 \dots, 13$, are elements of the reaction rate vector

$$\mathbf{S}(\mathbf{X}, V, W) = \begin{bmatrix} \lambda_i(t) \\ r_1(X_7, W)X_1 \\ r_2X_1X_2 \\ r_3(T_3 - X_4) \\ r_4X_3X_4 \\ r_5(T_4 - X_2 - X_3 - X_4) \\ r_6X_4 \\ r_7(X_7, W)X_4 \\ r_8(X_7, W)X_5 \\ r_9(X_8) \frac{(X_5)(X_5-1)}{2} (T_1 - X_6) \\ r_{10}(X_7, W)X_6 \\ r_{11}(T_2 - X_7)X_8 \\ r_{12}X_7 \end{bmatrix},$$

with $\lambda_i(t)$ the rate of photon arrival at microvillus i . The 12 rates correspond to the 12 reactions governing the phototransduction process and are given by [1]

$$\begin{aligned} r_1(X_7, W) &= -\gamma_{M^*} (1 + h_{M^*} f_n(X_7, W)) \\ r_2 &= -\kappa_{G^*} \\ r_3 &= \kappa_{PLC^*} \\ r_4 &= \gamma_{GAP} \\ r_5 &= \gamma_G \\ r_6 &= \kappa_{D^*} \\ r_7(X_7, W) &= \gamma_{PLC^*} (1 + h_{PLC^*} f_n(X_7, W)) \\ r_8(X_7, W) &= \gamma_{D^*} (1 + h_{D^*} f_n(X_7, W)) \\ r_9(X_8) &= \kappa_{T^*} (1 + h_{TRP^*,p} f_p(X_8)) \\ r_{10}(X_7, W) &= \gamma_{TRP^*} (1 + h_{TRP^*,n} f_n(X_7, W)) \\ r_{11} &= K_u \\ r_{12} &= K_R \end{aligned}$$

and

$$f_p(X_8) = \frac{(X_8/K_p)^2}{1 + (X_8/K_p)^2}, \quad (12)$$

$$f_n(X_7, W) = W \frac{\left(\frac{X_7}{N_{mol}K_n}\right)^3}{1 + \left(\frac{X_7}{N_{mol}K_n}\right)^3}, \quad (13)$$

where W denotes the strength of the global feedback from the photoreceptor membrane. W follows the dynamics

$$dW = \frac{W_\infty(V) - W}{\tau_W} dt, \quad (14)$$

where $\tau_W = 1$, and

$$W_\infty(V) = \begin{cases} 8.57(V + 53) + 5 & \text{if } v \geq -53 \\ \min(1, 0.2354(V + 70) + 1) & \text{otherwise} \end{cases}.$$

Note that r_1, r_7, r_8, r_9 and r_{10} are reaction rates that depend on the concentration of either X_7 or X_8 . Calcium dynamics are assumed to be fast enough such that they are fully captured by a steady state response. The calcium concentration can be expressed as

$$X_8^m = \min\left(\frac{\frac{I_{Ca}^m}{2 \cdot L \cdot F} + 4K_R \frac{X_7^m}{N_{mol}} + C_1}{4K_U \frac{T_2 - X_7^m}{N_{mol}} + K_{Ca} + C_2(V)}, 1.6 \times 10^{-4}\right) \quad (15)$$

where

$$C_1 = K_{NaCa} \frac{[Na^+]_i^3 [Ca^{2+}]_o}{L \cdot F}, \quad (16)$$

$$C_2(V) = K_{NaCa} \frac{\exp(-\frac{VF}{1000RT}) [Na^+]_o^3}{L \cdot F}, \quad (17)$$

with V denoting the membrane voltage of the photoreceptor, in millivolts, and (see also (18))

$$I_{Ca}^m = 0.4I^m.$$

Finally, the number of open TRP channels determines the light induced current that can be expressed as

$$I^m(t) = X_6^m \cdot g_{TRP} \cdot \max(V_{TRP,rev} - V, 0). \quad (18)$$

Assuming the photoreceptor is at resting state, the initial condition of (11) is

$$\mathbf{x}_0 = [0, T_4, 0, 0, 0, 0, 0]^T.$$

A full description of the parameters and constants is given in Table 2 in Appendix A. The total light induced current in the photoreceptor amounts to

$$I(t) = \sum_{m=1}^M I^m(t). \quad (19)$$

4.1.3 The Photo-Insensitive Cell Membrane Model

The photo-insensitive cell membrane of the photoreceptor is described by a conductance-based model. The circuit diagram of the conductance-based model is shown in Figure 14.

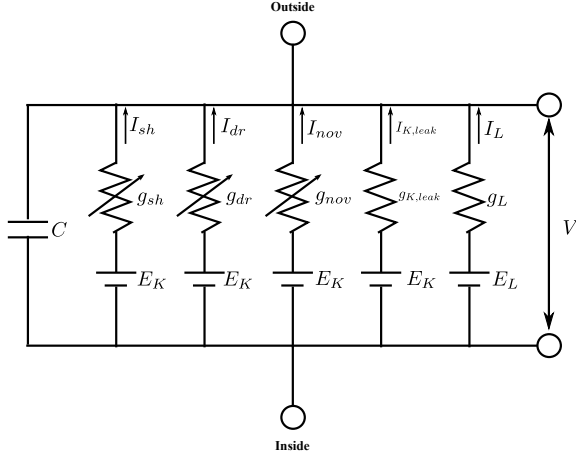


Figure 14: Circuit diagram of the conductance-based model of the photoreceptor photo-insensitive cell membrane. The equivalent circuit consists of a capacitor C , a voltage gated shaker K^+ channel with conductance g_{sh} , a voltage gated delayed rectifier, Shab, K^+ channel with conductance g_{dr} , a novel voltage gated K^+ channel with conductance g_{nov} , a potassium leak conductance $g_{K,leak}$ and a chloride leak conductance g_L .

The model consists of 5 conductance channels out of which 4 are various forms of potassium channels and one is a chloride leak channel. We will refer to the cell membrane state vector as \mathbf{Y} , where

$$\mathbf{Y} = [V, Y_2, Y_3, Y_4, Y_5, Y_6]^\top. \quad (20)$$

The cell membrane voltage model can be expressed by the system of differential equations [19, 1]

$$\frac{d\mathbf{Y}}{dt} = \mathbf{f}(\mathbf{Y}) + [I(t), \mathbf{0}]^\top, \quad (21)$$

where $\mathbf{0}$ is a row vector of length 5, and (21) can be expanded as

$$\begin{aligned}
 \frac{dV}{dt} &= (I(t) - g_{K,\text{leak}}(V - E_K) - g_L(V - E_{Cl}) \\
 &\quad - \bar{g}_A Y_2^3 Y_3 (V - E_K) - \bar{g}_{dr} Y_4^2 Y_5 (V - E_K) - \bar{g}_{nov} Y_6 (V - E_K)) / C \\
 \frac{dY_2}{dt} &= \frac{Y_{2,\infty}(V) - Y_2}{\tau_{Y_2}(V)} \\
 \frac{dY_3}{dt} &= \frac{Y_{3,\infty}(V) - Y_3}{\tau_{Y_3}(V)} \\
 \frac{dY_4}{dt} &= \frac{Y_{4,\infty}(V) - Y_4}{\tau_{Y_4}(V)} \\
 \frac{dY_5}{dt} &= \frac{Y_{5,\infty}(V) - Y_5}{\tau_{Y_5}(V)} \\
 \frac{dY_6}{dt} &= \frac{Y_{6,\infty}(V) - Y_6}{\tau_{Y_6}(V)},
 \end{aligned} \tag{22}$$

where

$$\begin{aligned}
Y_{2,\infty}(V) &= \left(\frac{1}{1 + \exp\left(\frac{-23.7-V}{12.8}\right)} \right)^{\frac{1}{3}} \\
\tau_{Y_2}(V) &= 0.13 + 3.39 \exp\left(-\left(\frac{-73-V}{20}\right)^2\right) \\
Y_{3,\infty}(V) &= \frac{0.9}{1 + \exp\left(\frac{-55-V}{-3.9}\right)} + \frac{0.1}{1 + \exp\left(\frac{-74.8-V}{-10.7}\right)} \\
\tau_{Y_3}(V) &= 113 \exp\left(-\left(\frac{-71-V}{29}\right)^2\right) \\
Y_{4,\infty}(V) &= \left(\frac{1}{1 + \exp\left(\frac{-1-V}{9.1}\right)} \right)^{\frac{1}{2}}, \\
\tau_{Y_4}(V) &= 0.5 + 5.75 \exp\left(-\left(\frac{-25-V}{32}\right)^2\right) \\
Y_{5,\infty}(V) &= \frac{1}{1 + \exp\left(\frac{-25.7-V}{-6.4}\right)} \\
\tau_{Y_5}(V) &= 890 \\
Y_{6,\infty}(V) &= \frac{1}{1 + \exp\left(\frac{-12-V}{11}\right)} \\
\tau_{Y_6}(V) &= 3 + 166 \exp\left(-\left(\frac{-20-V}{22}\right)^2\right)
\end{aligned}$$

with parameters

$$\begin{aligned}
E_K &= -85 \text{ mV}, \quad E_{Cl} = -30 \text{ mV}, \\
g_{K,leak} &= 0.082 \text{ mS/cm}^2, \quad g_L = 0.006 \text{ mS/cm}^2, \\
\bar{g}_A &= 1.6 \text{ mS/cm}^2, \quad \bar{g}_{dr} = 3.5 \text{ mS/cm}^2, \\
\bar{g}_{nov} &= 3.0 \text{ mS/cm}^2, \quad C = 4 \mu\text{F/cm}^2.
\end{aligned}$$

The initial condition of the system is set to the resting state. The above equations and parameters were obtained or estimated from [24, 25].

4.2 Implementation of the Photoreceptor Model

4.2.1 Implementation of Photo Absorption

Following the model of photon absorption described in Section 4.1.1, Algorithm 4 describes the implementation of the absorption of photons at a given time step.

Algorithm 4 Photon Absorption Algorithm

```

procedure UPDATE_INPUT_RATE( $\lambda^j(t)$ ,  $M$ ,  $\Delta t$ ,  $i$ )
     $\lambda_m^j \leftarrow \lambda^j(i \cdot \Delta t) / M$ 
end procedure

```

4.2.2 Implementation of the Phototransduction Process

For the phototransduction process, the Gillespie algorithm is employed to obtain a simulated trajectory from the master equations in (11). Since the number of molecules is small, the state variables of each microvillus can be stored as 7 16-bit integers.

At a given time in the simulation, the next reaction that takes place is chosen randomly based on the rate \mathbf{S} . The time until the next reaction is drawn from an exponential distribution with mean $1/\lambda_s$, where $\lambda_s = \sum_{n=1}^{13} S_n$ with S_n is the n th entry of \mathbf{S} . We then draw randomly η from the uniform distribution on $[0, \lambda_s]$, and the index of the next reaction i can be determined by

$$i = \operatorname{argmax}_{i=1,2,\dots,13} \left\{ \left(\sum_{n=1}^i S_n \right) \leq \eta \right\} - 1.$$

The change of the state variables \mathbf{x} due to the i th reaction, $i = 1, 2, \dots, 13$, is then simply a read out of \mathbf{b}_i , the i th column of the jump matrix \mathbf{B} . The state variables are then updated according to the i th reaction as

$$\mathbf{X}^m \leftarrow \mathbf{X}^m + \mathbf{b}_i.$$

The phototransduction process is described in Algorithm 5. Algorithm 5 provides an implementation of the chemical reactions through the Gillespie algorithm. Constants used in the algorithm are described in section A of the Appendix.

Algorithm 5 Phototransduction Algorithm

```

procedure TRANSDUCTION( $\mathbf{X}^m, \lambda_m^j(t), m = 1, \dots, M, \Delta t, V, W$ )
  for  $m \leftarrow 1, \dots, M$  do
     $t \leftarrow 0$ 
    while True do
      compute  $\mathbf{S}$ 
       $\lambda_s \leftarrow \sum_{n=1}^{13} S_n$ 
       $t_s \leftarrow \frac{1}{T_{la} + \lambda_s} \ln(1 / \text{rand}())$ 
       $t \leftarrow t + t_s$ 
      if  $t > \Delta t$  then
        break
      end if
       $\eta \leftarrow$  randomly draw uniformly from  $[0, \lambda_s]$ 
       $i \leftarrow \underset{i=1,2,\dots,13}{\text{argmax}} \left\{ \sum_{n=1}^i S_n \leq \eta \right\} - 1$ 
       $\mathbf{X}^m \leftarrow \mathbf{X}^m + \mathbf{b}_i$ 
    end while
  end for
   $I \leftarrow \sum_{m=1}^M X_6^m \cdot g_{TRP} \cdot \max(V_{TRP,rev} - V, 0)$ 
end procedure

```

4.2.3 Implementation of the Photo-Insensitive Cell Membrane

The system of differential equations in (22) is simulated using standard numerical methods for solving ODEs. Algorithm 6 describes the update of photoreceptor membrane potential using the forward Euler method.

Algorithm 6 Cell Body Model Algorithm

```

procedure CELL_BODY( $I, \mathbf{Y}, \Delta t$ )
     $\mathbf{Y} \leftarrow \mathbf{Y} + (\mathbf{f}(\mathbf{Y}) + [I, \mathbf{0}]^T) \Delta t$ 
end procedure

```

4.2.4 Overall Implementation of the Photoreceptor Model

Algorithm 7 describes the overall photoreceptor algorithm by combining Algorithms 4, 5 and 6.

Algorithm 7 Full simulation

```

procedure SIMULATION( $\lambda^j(t), N_{steps}, M, \Delta t$ )
    init ( ${}^j\mathbf{X}_0^m = \mathbf{x}_0, {}^j\mathbf{Y}, {}^jW$ )
    for  $i \leftarrow 1, \dots, N_{steps}$  do
         $\lambda_m^j \leftarrow update\_input\_rate(\lambda^j(t), M, \Delta t, i)$                                 ▷ Algorithm 4
         ${}^jI \leftarrow transduction({}^j\mathbf{X}^m, \lambda_m^j, m = 1, \dots, M, \Delta t, {}^jV, {}^jW)$       ▷ Algorithm 5
         $cell\_body({}^jI, {}^j\mathbf{Y}, \Delta t)$                                                  ▷ Algorithm 6
    end for
end procedure

```

4.2.5 Complexity of the Implementation

As already mentioned a typical photoreceptor has about 30,000 microvilli. By counting the 12 reactions as 12 equations and by adding (12), (13), (15), we obtain a total of 15 equations that govern the transduction in each microvillus. Therefore, a single photoreceptor is described by 450,006 equations (6 equations are from (22)). This amounts to approximately 2 billion equations for the entire eye with 721 ommatidia (without R7/R8).

Memory usage is dominated by the states of microvilli. The state of each microvillus is stored in 7 16-bit integer variables. A total of 30,000 microvilli per photoreceptor requires $30,000 \cdot 7 \cdot 2$ bytes = 420Kbytes. For 4,326 photoreceptors, the amount of memory used in simulations is about 1.8 Gbytes.

4.3 I/O Evaluation of the Photoreceptor Model

4.3.1 Simulation Time

The simulation of a single photoreceptor model was performed on a Nvidia Kepler K20X GPU with 6 GB of memory. The simulation time of the response of a single photoreceptor to a 1 second long visual field with an average luminance of 300,000 photons/s was 5.7 seconds.

4.3.2 Transient and Steady State Responses to Constant Inputs

We evaluated the response of a single photoreceptor to constant inputs. Typical inputs are shown in Figure 15a. The onset of the constant input takes place at $t = 0.5$ s. The photoreceptor responses are shown in Figure 15b.

The photoreceptor responds strongly to the onset of a constant stimulus before gradually settling to a steady state value. The steady state response is approximately log-linear w.r.t. the number of input photons in a range of 1,000-fold luminance change, as shown in Figure 15c.

4.3.3 Response to Natural Stimuli

We presented to the photoreceptor a natural stimulus sequence with several levels of mean luminance values. The input and the corresponding response are shown in Figure 16. While the response to mean luminance values is log-linear to several input magnitudes ranges (see Figure 15c), the temporal contrast of the model response is constant over 3 magnitudes of mean luminance levels.

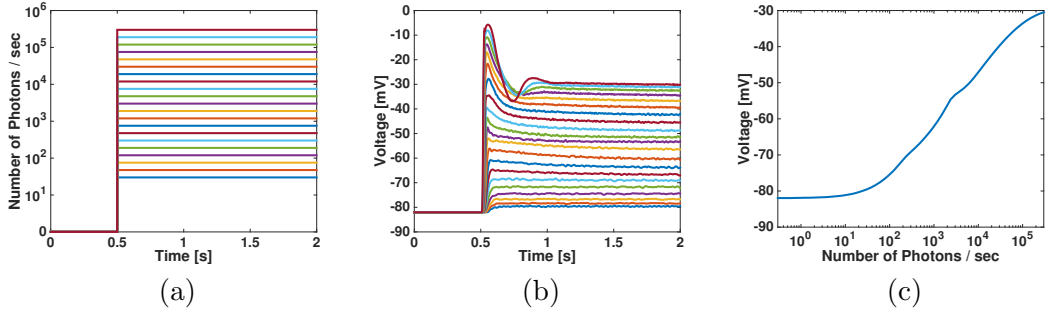


Figure 15: (a) Photoreceptor inputs with onset at 0.5 seconds. The light intensity is equally spaced on the logarithmic scale. (b) Response of a photoreceptor to the inputs in (a). Response curves are shown in the same color as the corresponding input ones. (c) The steady state response to a constant light intensity is approximately log-linear with respect to the input intensity over 4 orders of magnitude.

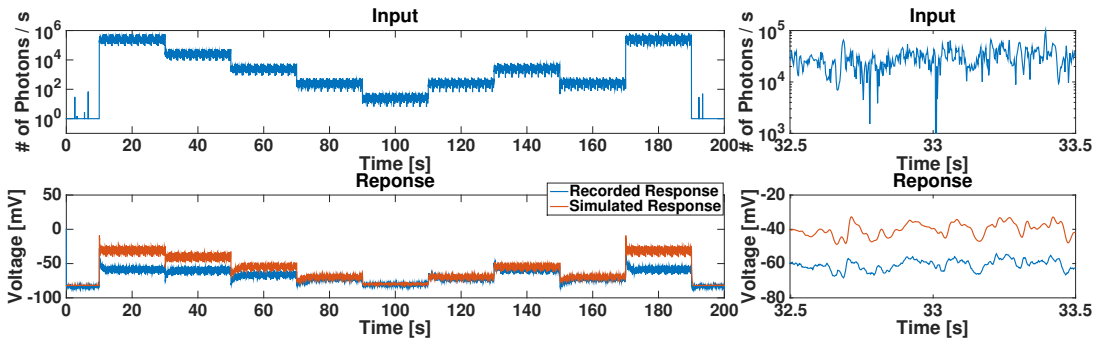


Figure 16: Response of the photoreceptor model to natural stimuli. (Top) Input stimulus spanning several different magnitude levels. One second of the input is magnified on the right. (Bottom) Response of the photoreceptor model (red) and recorded response (blue) to natural stimuli. One second of the response is magnified on the right. (Recording data from <http://www.dflybrain.org>)

5 The Retina as a Parallel Information Pre-Processor

This section is organized as follows. In section 5.1 the entire Retina is modeled as a Local Processing Unit (LPU). In section 5.2 an architecture that enables the efficient execution of the Retina LPU is presented. The implementation of the Retina LPU enables the visual evaluation of the effect of pre-processing taking place in the Retina. It also provides realistic inputs to models of subsequent neuropils in the early visual system of the fruit fly. Finally, in section 5.3 the evaluation of the LPU model are discussed.

5.1 Executing the Retina LPU in the Neurokernel

Here we model the Retina as a Local Processing Unit (LPU) that can be executed within the Neurokernel architecture. The Retina LPU consists of 721 ommatidia hosting a total of 4,326 photoreceptors. As a visual information pre-processor, the Retina LPU takes natural or artificial input videos mimicking the visual field of the fruit fly. The geometry of the Retina is as described in Section 3, and each photoreceptor has its own receptive field. The I/O of each photoreceptor is modeled as described in Section 4. Finally, the outputs of the Retina LPU are the membrane potentials of the 4,326 photoreceptors.

In order to communicate with subsequent visual LPUs under the Neurokernel platform, the Retina LPU exposes the following ports to the Neurokernel interface. We named the ports associated with each photoreceptor as a string

```
'ret/ommat<omm_id>/R<photor_id>'
```

where $\langle \text{omm_id} \rangle$ is the index number of an ommatidium given by (10), ranging from 0 to $N - 1$ where N is the number of ommatidia. The numbering of the ommatidia was described in Section 3.3.1. $\langle \text{photor_id} \rangle$ is the identifier ranging from 1 to 6 that corresponds to, respectively, R1 to R6. A total of 4,326 ports are exposed.

5.2 Distributing the Computation on Multiple GPUs

The Retina LPU employs massively parallel computation for the transduction and pre-processing of visual stimuli. The parallelism takes place on two levels. On the level of the eye, thousands of photoreceptors sample the visual space in parallel. On

the photoreceptor level, 30,000 microvilli carry out the transduction of light intensity into current intensity and the temporal processing of the resulting current.

As stated in Section 4.2.5, the entire fruit fly Retina LPU is modeled by approximately 2 billion equations. This intense computational demand calls for executing the Retina model in a massively parallel computing environment. The massively parallel computation of the Retina model is executed within the Neurokernel framework on a cluster of GPUs [6].

The highly parallel Retina LPU allows for splitting the computation across multiple GPUs. Figure 17 illustrates the distribution of the computational load onto multiple GPUs and the overall execution model of the Retina LPU on Neurokernel’s compute plane. The Retina LPU is executed on a master GPU and several worker GPUs. The master GPU communicates with the disc I/O and the inter-LPU communication mechanism, and performs the computation to generate visual inputs to the photoreceptors. The visual inputs are then split and passed to the worker GPUs to offload the computation required in the implementation of phototransduction process. After the worker GPUs update the states of the membrane potential of the photoreceptors, these values are gathered by the master GPU.

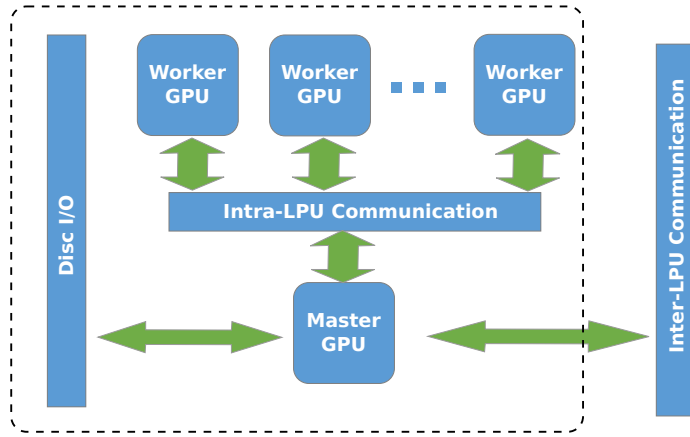


Figure 17: Execution model of the Retina LPU on the compute plane of the Neurokernel and the distribution of computation onto multiple GPUs.

In table 1, we show the time to simulate 1 second of the full scale Retina on 1, 2, and 4 Kepler K20X GPUs interconnected by a PCIe 2.0 bus. The speedup from splitting the work to multiple GPUs is almost ideal, since interactions between GPUs is minimal. This suggests that the Retina LPU is highly scalable over multiple GPUs.

Table 1: Performance metrics with different number of GPUs

	1 GPU	2 GPUs	4 GPUs
simulation time (sec)	120.9	64.4	38.0

5.3 Visual Evaluation of the Overall Response of the Retina

In this section we will examine the output of the Retina to natural stimuli. We continue to use visual scenes from Van Hateren’s database [18] and simulate the visual input perceived by a moving fly by using the image enclosed by a moving circular (red) window.

5.3.1 Visual Characterization of the Photoreceptors

The visual scene and the moving window are shown on the top left of the video of Figure 18. The visual scene is linearly scaled by mapping the value of the scene 0 to black (0) and mapping its maximum value to white (255). We also show a logarithmically companded scene on the top right in the same video. Note that the logarithm of the scene was not used in the simulation. The logarithm of the scene is scaled by mapping the minimum value of the logarithm of the scene to black (0) and by mapping the maximum value of the logarithm of the scene to white (255).

In the lower half of the video in Figure 18, we show two rows of images. The first column shows the visual field of the moving circular window and the logarithm of it; the mapping of values to black and white follows the mapping of the visual scene and the mapping of logarithm of the visual scene, respectively. The second column shows the input to all the R1 photoreceptor in terms of the number of photons. The minimum number of photons during the simulation is mapped to black (0) and the maximum is mapped to white (255). The third column shows a delayed version of the input and its logarithm; the delay is set to 40 milliseconds.

The response of all R1 photoreceptors is shown in the top circle in column 4. Here, the minimum voltage of all photoreceptors in the Retina during the simulation is mapped to black (0) and the maximum is mapped to white (255). The responses of all R2, R3, R4, R5 and R6 photoreceptors are similarly shown in the rest of the circles.

It can be seen that the natural visual scene in the linear range (of the number of photons) is dark and features a low intensity range that is not well perceived due

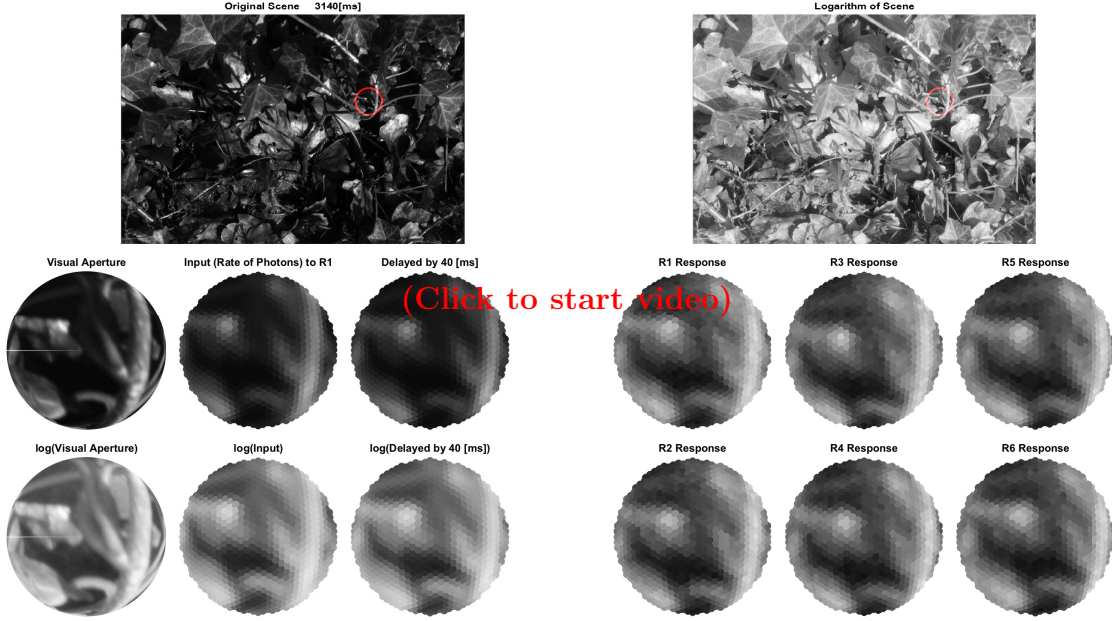


Figure 18: Visual evaluation of the fruit fly retina photoreceptors. (top left) Original scene. The red circle indicates the visual aperture of the eye. (top right) Logarithm of the original scene. (bottom left) “Visual Aperture” shows the projection of the area inside the red circle in the original scene onto the hemispherical visual field. “Input to R1” shows the rate of photons arriving at the R1 photoreceptors. “Delayed by 40 [ms]” shows the “Input to R1” delayed by 40 [ms]. “log(Visual Aperture)”, “log(Input)” and “log(Delayed by 40 [ms])” shows the log of the plot in, respectively, “Visual Aperture”, “Input to R1” and “Delayed by 40 [ms]”. Note that “Input to R1” is the actual input to the photoreceptors. (bottom right) The responses of photoreceptors R1-R6, respectively. All hemispheres are viewed orthogonal to their base plane. As a result, they appear to be circular. (To enable the video, see Supplementary Videos in Section 6.)

to the lack of contrast. On the contrary, more details in the logarithm of the scene are visible. Taking the logarithm of the scene is also similar to applying a gamma correction to the scene [26]. The latter is often employed in photography and image encoding to optimize bit usage.

We also note that the responses of the R1 and R3 photoreceptors shown in Figure 18 are slightly shifted from each other. A similar shift is observed between the responses of any other pairs of photoreceptors. This is due to the different optical axes of the R1 to R6 photoreceptors located in the same ommatidium, as shown in Figure 7b. Since we depict in Figure 18 the response of photoreceptors at the location of their residing ommatidia, the center of the photoreceptors' receptive fields appear slightly shifted from each other.

In order to see the details of the temporal evolution of the responses of photoreceptors, the videos in Figure 18 are played back at 1/10 speed in Figure 19. In section 5.3.3 we will compare the medium speed responses with the responses to motion of higher speed (see also Figure 23).

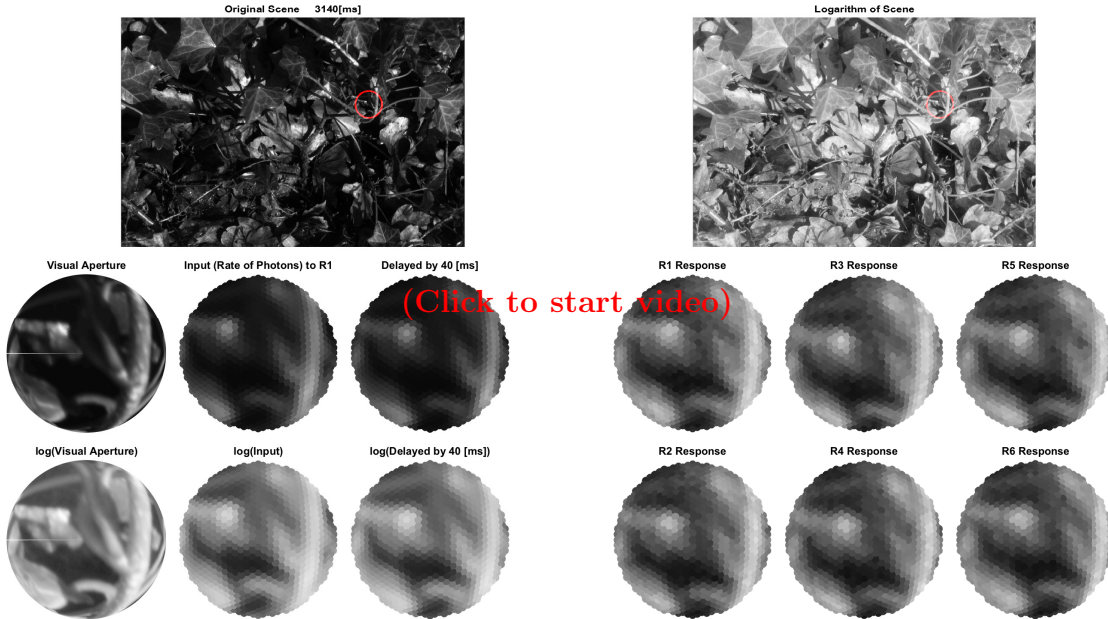


Figure 19: The video in Figure 18 at 1/10 of the real time playback speed. (To enable the video, see Supplementary Videos in Section 6)

5.3.2 The Effect of Mean Luminance on the Retina Output

We then examine the effect of different mean luminance on the Retina output. We scaled up and down the natural visual scene by a 10 fold and thereby scaled up and down the mean luminance. We refer to the scaled down version of the stimulus as the low luminance scene, the original version of the stimulus as the medium luminance scene and the scaled up version of the stimulus as the high luminance scene.

The response of the Retina to low luminance scenes is shown in the video of Figure 20. Note that since the scaling of the scene into black and white values is relative, the visual scene in Figure 20 looks very similar to the one in Figure 18 despite the fact that they differ by 10 fold factor. The same scaling applies to the logarithm of the scene and the inputs to the photoreceptors.

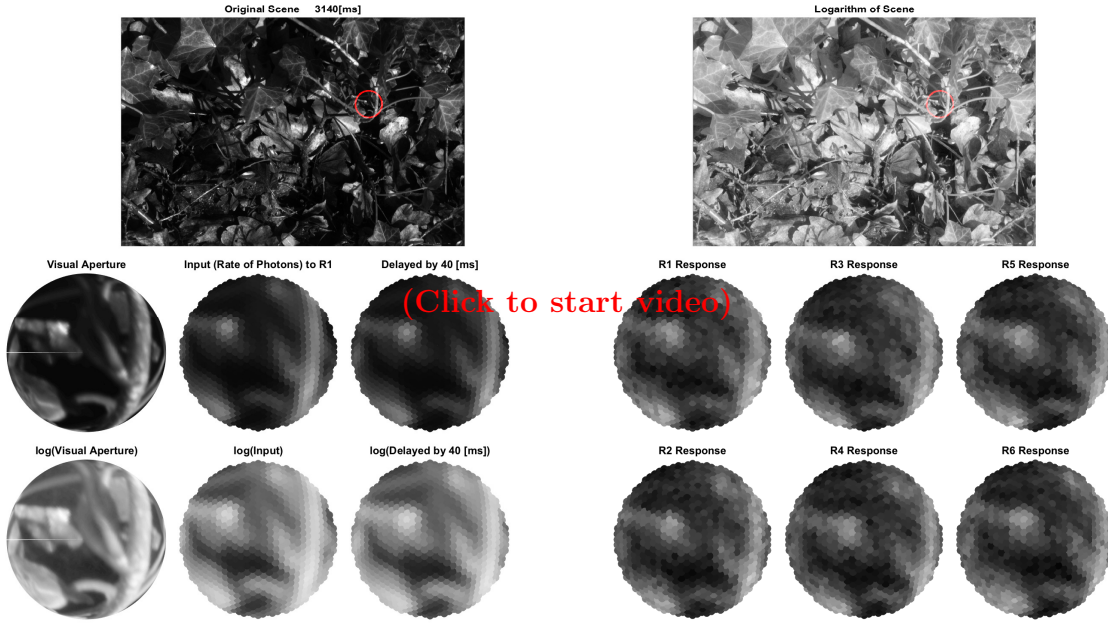


Figure 20: Retina response at low luminance level. (To enable the video, see Supplementary Videos in Section 6)

The Retina output in the low luminance scene has a similar linear range compared to that in the medium luminance scene, suggesting that although the preprocessing in different photoreceptors is independent, the aggregated spatial effect is an improved spatial contrast over a wide range of luminance levels. This pre-processing enables the processing in the later stages of the early visual system to operate within a spatial

set of contrast values that belongs to a controlled range.

At low luminance level, however, the response is visibly noisier. When compared with the input, the response of the Retina exhibits certain delays. In the video of Figure 21, we compare the responses at medium and low luminance levels side by side. The delay is slightly longer under low luminance levels than under medium luminance levels. This suggests a non-linear pre-processing in the Retina as a function of luminance levels. At lower luminance levels, the effect of noise on the Retina response is stronger. This calls for integrating the stimulus over longer time periods (delay) to reduce noise. Under better mean luminance conditions, the pre-processing in the Retina exhibits a faster response.

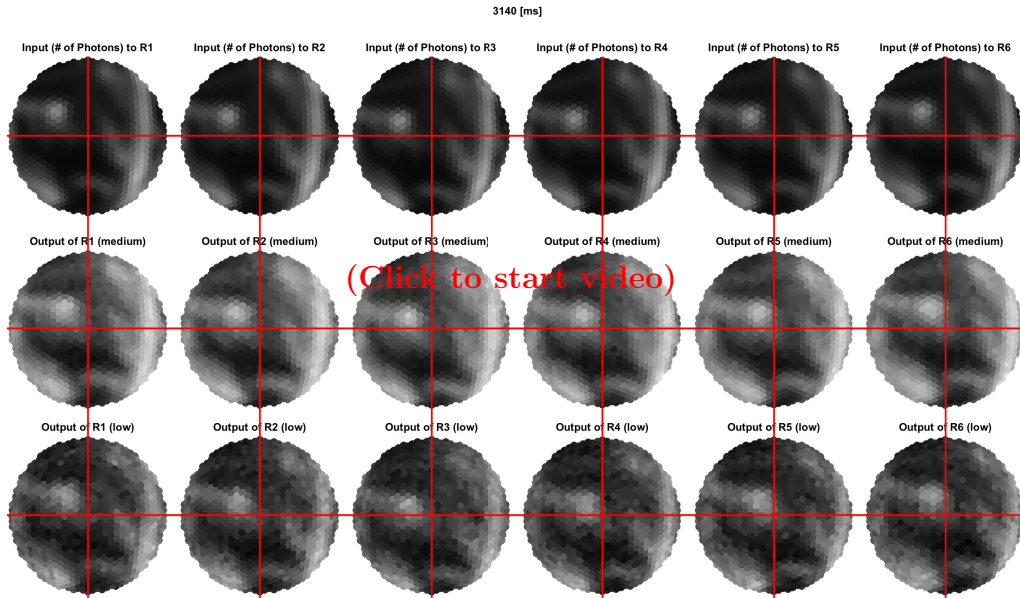


Figure 21: Comparison between responses under medium and low luminance conditions. First row shows the inputs at medium luminance level to R1, R2, R3, R4, R5 and R6 photoreceptors, respectively. The second row shows the responses of the corresponding photoreceptors in the medium luminance scene. The third row shows the responses of the corresponding photoreceptors in the low luminance scene. Grid lines (red) are added for an easier comparison of the responses across luminance levels. (To enable the video, see Supplementary Videos in Section 6)

The response of the Retina to high luminance scene is shown in the video of Figure 22.

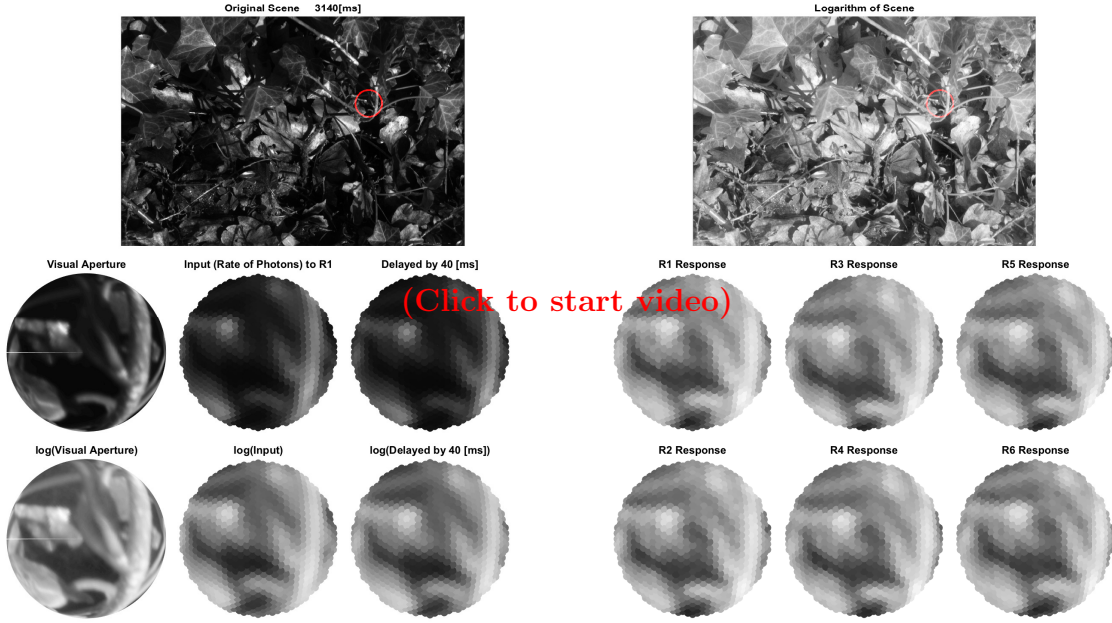


Figure 22: Retina response at high luminance level. (To enable the video, see Supplementary Videos in Section 6)

5.3.3 The Effect of the Speed of Motion on the Retina Output

Motion of higher speed can create motion blur due to insufficient bandwidth of the sampling units. We examine next the effect of increased motion speed on the overall Retina output. The response is shown in the video of Figure 23. Spatially, much less details can be seen in the response of the Retina as a result of faster motion. This can be seen by comparing the frame at 6,040 [ms] in the video of Figure 19 with the frame at 3,040 [ms] in the video of Figure 23. The visual inputs in the two cases are similar but the responses are different in that the leaf and the stem in the response to the fast motion scene is not discernible. However, it is still possible to detect the motion from the response. This suggest that motion detection at higher speed of motion can use less detailed spatial information than in the case of lower speed of motion.

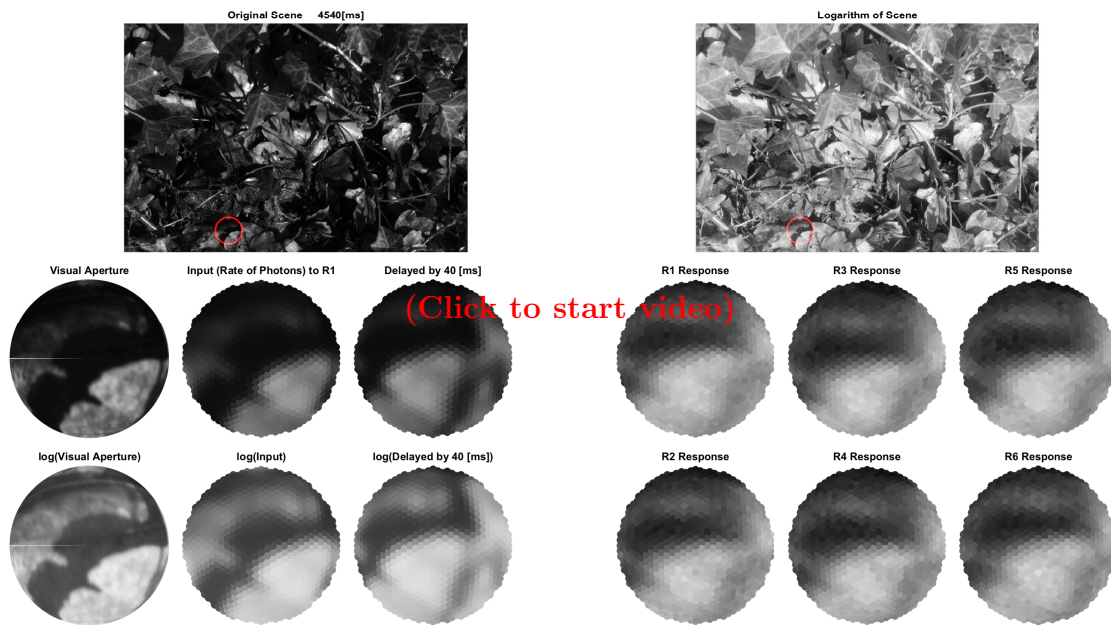


Figure 23: Retina response at a medium luminance level played out 5 times faster than in Figure 18. The video is played back at 1/10 of real time. (To enable the video, see Supplementary Videos in Section 6)

6 Supplementary Videos

To enable the videos marked in this PDF file, please follow the following steps

1. Download all the videos by clicking [here](https://drive.google.com/file/d/0Bw2dULm-npzzazdlc1NfQkpGaOU/view?usp=sharing) or using <https://drive.google.com/file/d/0Bw2dULm-npzzazdlc1NfQkpGaOU/view?usp=sharing>
2. Decompress the zip file into a folder named “videos” in the same directory as this PDF file.
3. Open this PDF file in Adobe Reader and click on the figure/video.

7 Acknowledgements

The research reported here was supported by AFOSR under grant #FA9550-12-1-0232.

References

- [1] Zhuoyi Song, Marten Postma, Stephen Billings, Daniel Coca, Roger C. Hardie, and Mikko Juusola. Stochastic, adaptive sampling of information by microvilli in fly photoreceptors. *Current Biology*, 22:1371–1380, 2012.
- [2] Uwe Friederich, Stephen A. Billings, Mikko Juusola, and Daniel Coca. We now know what fly photoreceptors compute. *BMC Neuroscience*, 14(Suppl 1):O5, 2013.
- [3] Kuno Kirschfeld. Die projektion der optischen umwelt auf das raster der rhabdomere im komplex auge von musca. *Experimental Brain Research*, 3:248–270, 1967.
- [4] Mikko Juusola and RC Hardie. Light adaptation in drosophila photoreceptors i. response dynamics and signaling efficiency at 25° c. *The Journal of general physiology*, 117(January), 2001.
- [5] Roger C. Hardie and Mikko Juusola. Phototransduction in *Drosophila*. *Current Opinion in Neurobiology*, 34:37–45, 2015.
- [6] Lev E. Givon and Aurel A. Lazar. Neurokernel: An open scalable software framework for emulation and validation of drosophila brain models on multiple GPUs. *Neurokernel RFC #1*, pages 1–23, 2014.
- [7] Martin Heisenberg and Reinhard Wolf. *Vision in Drosophila: Genetics of Microbehavior*. Springer, Berlin, 1984.
- [8] I. A. Meinertzhagen and S. D. O’Neil. Synaptic organization of columnar elements in the lamina of the wild type in *Drosophila melanogaster*. *The Journal of Comparative Neurology*, 305:232–263, 1991.
- [9] Donald Ready, Thomas Hanson, and Seymour Benzer. Development of the *Drosophila* retina, a neurocrystalline lattice. *Developmental Biology*, 53:217–240, 1976.
- [10] Roger C. Hardie and Padinjat Raghu. Visual transduction in *Drosophila*. *Nature*, 413(6852):186–193, Sep 2001.
- [11] T. Wolff and D. F. Ready. Pattern formation in the *Drosophila* retina. In *The Development of Drosophila melanogaster*, pages 1277–1325. Cold Spring Harbor Laboratory Press, 1993.

- [12] Roger C. Hardie. Functional organization of the fly retina. *Progress in Sensory Physiology*, 5:1–79, 1985.
- [13] Doekele G Stavenga and Kentaro Arikawa. One rhodopsin per photoreceptor: Iro-C genes break the rule. *PLoS Biology*, 6(4):e115, 04 2008.
- [14] John Snyder. Map projections - a working manual. *U.S. Geological Survey Professional Paper*, 1395, 1987.
- [15] Michael B. Reiser and Michael H. Dickinson. A modular display system for insect behavioral neuroscience. *Journal of Neuroscience Methods*, 167:127–139, 2008.
- [16] Michael F. Land. Visual acuity in insects. *Annual Review of Entomology*, 42(46):147–177, 1997.
- [17] Paloma T Gonzalez-Bellido, Trevor J Wardill, and Mikko Juusola. Compound eyes and retinal information processing in miniature dipteran species match their specific ecological demands. *Proceedings of the National Academy of Sciences of the United States of America*, 108(10):4224–4229, 2011.
- [18] J. H. Van Hateren and A. Van Der Schaaf. Independent component filters of natural images compared with simple cells in primary visual cortex. *Proceedings: Biological Sciences*, 265(1394):359–366, 1998.
- [19] Zhuoyi Song, Daniel Coca, Stephen Billing, Marten Postma, Roger C. Hardie, and Mikko Juusola. Biophysical modeling of a *Drosophila* photoreceptor. *ICONIP 2009, Part I, LNCS 5863*, pages 57–71, 2009.
- [20] Ben Katz and Baruch Minke. *Drosophila* photoreceptors and signaling mechanisms. *Frontiers in Cellular Neuroscience*, 3(2):1–8, 2009.
- [21] Marten Postma and Roger C. Hardie. *Phototransduction in microvillar photoreceptors of Drosophila and other invertebrates. The Senses: A Comprehensive Reference*, volume 1, chapter 5, pages 77–130. Academic Press, 2008.
- [22] Roger C Hardie. Phototransduction in *Drosophila melanogaster*. *Journal of Experimental Biology*, 3409:3403–3409, 2001.
- [23] Daniel T. Gillespie. Stochastic simulation of chemical kinetics. *Annual Review of Physical Chemistry*, 58:35–55, 2007.
- [24] Jeremy E. Niven, Mikko Vähäsöyrinki, Mika Kauranen, Roger C. Hardie, Mikko

- Juusola, and Matti Weckström. The contribution of *Shaker* K⁺ channels to the information capacity of *Drosophila* photoreceptors. *Nature*, 421:630–634, 2003.
- [25] Mikko Vähäsöyrinki, Jeremy E. Niven, Roger C. Hardie, Matti Weckström, and Mikko Juusola. Robustness of neural coding in *Drosophila* photoreceptors in the absence of slow delayed rectifier K⁺ channels. *Journal of Neuroscience*, 26(10):2652–2660, 2006.
- [26] Christophe Schlick. Quantization techniques for visualization of high dynamic range pictures. In *Photorealistic Rendering Techniques*, pages 7–20. Springer Berlin Heidelberg, 1995.
- [27] Cornelia A Hofstee, Stephen Henderson, Roger C Hardie, and Doekele G Stavenga. Differential effects of ninaC proteins (p132 and p174) on light-activated currents and pupil mechanism in drosophila photoreceptors. *Visual Neuroscience*, 13(5):897–906, 1996.
- [28] M. Postma, J. Oberwinkler, and D. G. Stavenga. Does Ca²⁺ reach millimolar concentrations after single photon absorption in *Drosophila* photoreceptor microvilli? *Biophysical Journal*, 77(4):1811–1823, Oct 1999.
- [29] J. A. Porter, M. Yu, S. K. Doberstein, T. D. Pollard, and C. Montell. Dependence of calmodulin localization in the retina on the NINAC unconventional myosin. *Science*, 262(5136):1038–1042, Nov 1993.
- [30] A. Huber, P. Sander, A. Gobert, M. Bahner, R. Hermann, and R. Paulsen. The transient receptor potential protein (Trp), a putative store-operated Ca²⁺ channel essential for phosphoinositide-mediated photoreception, forms a signalling complex with NorpA, InaC and InaD. *EMBO Journal*, 15(24):7036–7045, Dec 1996.
- [31] A. Pumir, J. Graves, R. Ranganathan, and B. I. Shraiman. Systems analysis of the single photon response in invertebrate photoreceptors. *Proc. Natl. Acad. Sci. U.S.A.*, 105(30):10354–10359, Jul 2008.

A Parameters Used in the Retina LPU Implementation

Table 2: Phototransduction Constants

Constant Name	Value	Description	Origin
$[Na^+]_o$	120 mM	Extracellular sodium concentration	[27]
$[Na^+]_i$	8 mM	Intracellular sodium concentration	[28]
$[Ca^{2+}]_o$	1.5 mM	Extracellular calcium concentration	[27]
T_2	903	Total number of calmodulin	[29]
T_4	50	Total number of G-protein	[10]
T_3	100	Total number of PLC	[30]
T_1	25	Total number of TRP/TRPL channels	[30]
γ_{D^*}	4.0 s^{-1}	Deactivation rate of D*	[1]
γ_G	3.0 s^{-1}	Deactivation rate of G-protein by GTPase activity	[1]
γ_{GAP}	3.5 s^{-1}	Conversion rate from $G_\alpha\text{GDP}$ to G-protein	[1]
γ_{M^*}	3.7 s^{-1}	Deactivation rate of M*	[31]
γ_{PLC^*}	144 s^{-1}	Deactivation rate of PLC*	[1]
γ_{TRP^*}	25 s^{-1}	Deactivation rate of TRP/TRPL channels	[1]
h_{D^*}	37.8	Strength of negative calmodulin feedback to D*	[31]
h_{M^*}	40	Strength of negative calmodulin feedback to M*	[1]
h_{PLC^*}	11.1	Strength of negative calmodulin feedback to PLC*	[31]
$h_{TRP^*,p}$	11.5	Strength of negative calcium feedback to T*	[1]
$h_{TRP^*,n}$	10	Strength of negative calmodulin feedback to T*	[1]
K_p	0.3 mM	Dissociation coefficient for calcium positive feedback	[1]

Continued on next page

Table 2: Phototransduction Constants

Constant Name	Value	Description	Origin
K_n	0.18 mM	Dissociation coefficient for calmodulin negative feedback	[1]
K_U	$30 \text{ mM}^{-1} \text{ s}^{-1}$	Rate of Ca^{2+} uptake by calmodulin	[31]
K_R	5.5 s^{-1}	Rate of Ca^{2+} release by calmodulin	[31]
K_{Ca}	1000 s^{-1}	Rate of Ca^{2+} diffusion from microvillus to somata	[1]
K_{NaCa}	$3 \cdot 10^{-8}$	Scaling factor for $\text{Na}^+/\text{Ca}^{2+}$ exchanger model	[1]
κ_{D^*}	1300 s^{-1}	rate of D* activation	[1]
κ_{G^*}	7.05 s^{-1}	rate of G* activation	[1]
κ_{PLC^*}	15.6 s^{-1}	rate of TRP/TRPL channels activation	[1]
κ_{TRP^*}	150 s^{-1}	rate of T* activation	[1]
K_{D^*}	100	Transition rate from D* to opening of TRP/TRPL channels	[1]
F	96 485 mC/mol	Faraday constant	known constant
N	4	binding sites for calcium on calmodulin	[1]
R	$8.314 \text{ J K}^{-1} \text{ mol}^{-1}$	gas constant	known constant
T	293 K	absolute temperature	known constant
L	$3 \times 10^{-9} \text{ nl}$	microvillus volume	known constant
g_{TRP}	8 pS	conductance of a TRP channel	[1]
$V_{TRP,rev}$	0	TRP channel reversal potential	[1]
T_{la}	0.5	latency regulator	[1]

Based on the Volume of the microvilli, 1 mM corresponds to 1806 molecules. That is $N_{mol} = 1806$.